AGU PUBLICATIONS

JGR

Journal of Geophysical Research: Solid Earth

RESEARCH ARTICLE
10.1002/2015JB012064

Key Points:
- Phase transitions and mantle layering
- The impact of the perovskite-postperovskite phase transition on mantle mixing
- The impact of the iron spin transition in the lower mantle on mantle mixing

Correspondence to:
M. H. Shahnas,
shahnas@atmosp.physics.utoronto.ca

Citation:
Shahnas, M. H., and W. R. Peltier (2015), The impacts of mantle phase transitions and the iron spin crossover in ferropericlase on convective mixing—is the evidence for compositional convection definitive? New results from a Yin-Yang overset grid-based control volume model, *J. Geophys. Res. Solid Earth*, *120*, 5884–5910, doi:10.1002/2015JB012064.

Received 24 MAR 2015
Accepted 21 JUL 2015
Accepted article online 25 JUL 2015
Published online 22 AUG 2015

The impacts of mantle phase transitions and the iron spin crossover in ferropericlase on convective mixing—Is the evidence for compositional convection definitive? New results from a Yin-Yang overset grid-based control volume model

M. H. Shahnas[1] and W. R. Peltier[1]

[1]Department of Physics, University of Toronto, Toronto, Ontario, Canada

Abstract High-resolution seismic tomographic images from several subduction zones provide evidence for the inhibition of the downwelling of subducting slabs at the level of the 660 km depth seismic discontinuity. Furthermore, the inference of old (~140 Myr) sinking slabs below fossil subduction zones in the lower mantle has yet to be explained. We employ a control volume methodology to develop a new anelastically compressible model of three-dimensional thermal convection in the "mantle" of a terrestrial planet that fully incorporates the influence of large variations in material properties. The model also incorporates the influence of (1) multiple solid-solid pressure-induced phase transitions, (2) transformational superplasticity at 660 km depth, and (3) the high spin-low spin iron spin transition in ferropericlase at midmantle pressures. The message passing interface-parallelized code is successfully tested against previously published benchmark results. The high-resolution control volume models exhibit the same degree of radial layering as previously shown to be characteristic of otherwise identical 2-D axisymmetric spherical models. The layering is enhanced by the presence of moderate transformational superplasticity, and in the presence of the spin crossover in ferropericlase, stagnation of cold downwellings occurs in the range of spin crossover depths (~1700 km). Although this electronic spin transition has been suggested to be invisible seismically, recent high-pressure ab initio calculations suggest it to have a clear signature in body wave velocities which could provide an isochemical explanation of a seismological signature involving the onset of decorrelation between V_p and V_s that has come to be interpreted as requiring compositional layering.

1. Introduction

Radial heat transfer in the interior of the Earth and other terrestrial planets plays a vital role in the thermal evolution of these objects, in the maintenance of their magnetic fields, and, in the case of Earth, in forcing the "drift" of the surface continents relative to one another. Especially for the Earth, in which radial heat transfer is dominated by solid-state thermal convection, the ability to accurately simulate this process is essential to our ability to understand the evolutionary trajectory of the object since it first formed approximately 4.56 billion years ago. Because the process of solid-state convection in the "mantle" of the Earth which surrounds its liquid iron outer core is a hydrodynamic phenomenon and because the effective viscosity of a "solid" is controlled by a thermally activated solid-state creep mechanism, it is expected that thermal convective mixing in a system of this kind will involve large variation in effective viscosity. Given that the core-mantle boundary (CMB) interface, is at present at a temperature T_{CMB} such that $3600°K \leq T_{CMB} \leq 4000°K$ [e.g., *Boehler*, 1992] and given that the mantle of the Earth is extremely thick, with its depth $d \approx 2900$ km and that its effective viscosity, in an azimuthally averaged depth-dependent sense, is in the vicinity of 10^{21} Pa·s [e.g., *Peltier*, 1998a], the effective Rayleigh number that determines the efficiency of radial heat transfer is found to be on the order of 10^7 [e.g., *Jarvis and Peltier*, 1982]. Since this is approximately 10^4 times the nominal critical value for the onset of convection, it is clear that the circulation in this system will be determined by thin thermal boundary layers and strongly localized thermal upwellings (plumes) and downwellings characterized by large lateral variations of effective viscosity.

The numerical challenge that must be met in the accurate representation of the mixing process in a system of this kind is therefore significant. Not only are the physical properties of the assemblage of minerals that make

up the solid expected to be strong functions of temperature and pressure, but there also exists a series of pressure-induced phase transitions that occur in the mineral assemblage as depth in the system, and thus hydrostatic pressure increases. The earliest numerical models that were developed in an attempt to provide an understanding of mantle mixing were based upon the application of simple second-order accurate finite difference (FD) methods [*Turcotte and Oxburgh*, 1967; *Torrance and Turcotte*, 1971; *Peltier*, 1972; *McKenzie et al*., 1974; *Parmentier et al*., 1975; *Jarvis and McKenzie*, 1980; *Yuen and Peltier*, 1980; *Jarvis and Peltier*, 1982] and typically incorporated none of the above enumerated complexities. In this early work, the value of the diffusivity for momentum, υ, was recognized to be so large relative to the thermal diffusivity, κ, that the Prandtl number $\mathrm{Pr} = \upsilon/\kappa$ was such that $\mathrm{Pr} \geq 10^{20}$, implying that the action of the inertial force would be entirely negligible relative to the viscous force, thus rendering these flows quasistatic. The high Rayleigh number circulation is therefore expected to be thermally, but not mechanically, turbulent.

More recent advances in the development of models of the mantle convection process have most often been based upon the finite element methodology [e.g., *Christensen*, 1984; *Christensen and Yuen*, 1989; *Baumgardner*, 1985; *King et al*., 1990; *Moresi and Gurnis*, 1996; *Bunge et al*., 1997; *Zhong et al*., 2000]. This methodology has proven to be more effective than the simpler FD formulation in the sense that it is more capable of dealing with large variations of physical properties or in circumstances in which the geometry is assumed to be irregular.

Spectral methods [*Honda et al*., 1993] have also been applied to the mantle convection problem as these are known to possess significant advantages insofar as accuracy is concerned, at least in circumstances in which rheological complexity is irrelevant. Until recently, these methods have remained the basis of the technology of choice in the numerical representation of the general circulation of the atmosphere as this is embedded within the multicomponent structure of a modern coupled climate model [e.g., the NCAR CCSM3/4 structure, *Collins et al*., 2006]. As originally developed by *Orszag* [1969], the method is typically implemented in what is termed a "semispectral" mode in which the hydrodynamic fields are time stepped in the wave number domain of the set of spherical harmonic basis functions in terms of which the fields are expanded. The nonlinear advection terms are evaluated in physical space and then transformed back to the wave number domain prior to each time advance of the model. The availability of the fast Fourier transform algorithm for the longitude dependence of the fields on each latitude circle and of accurate Gaussian quadrature for evaluation of the latitudinal part of the transform dramatically improves the efficiency of this method, especially in circumstances in which the spatial resolution is modest [see *Stuhne and Peltier*, 1999, for a discussion of issues concerning the behavior of this methodology at extremely high spatial resolution]. A great deal of effort has been devoted to the implementation of spectral methods in the mantle convection context [e.g., *Glatzmaier*, 1988; *Machetel et al*., 1995; *Monnereau and Quere*, 2001; *Forte and Peltier*, 1994; *Tackley et al*., 1994; *Zhang and Christensen*, 1993; *Zhang and Yuen*, 1996]. A significant problem with this methodology, however, concerns its limitations insofar as enabling the analysis of flows with azimuthal variations of viscosity to be accurately performed [*Balachandar et al*., 1996; *Christensen and Harder*, 1991; *Zhang and Christensen*, 1993]. Because of this problem, such methods have normally been restricted to the investigation of the mantle convection process subject to the assumption that viscosity is a function of depth alone, in which case the depth dependence has usually been represented using finite differences [e.g., *Machetel et al*., 1986; *Glatzmaier*, 1988; *Balachandar and Yuen*, 1994]. *Glatzmaier* [1988] in fact employed Chebyshev representations to resolve the radial structure of each dependent variable, and *Balachandar and Yuen* [1994] employed a stretched Chebyshev representation.

One of the most efficient methodologies for application to the convection problem, in principle, in circumstances in which there exist large variations of physical properties, both azimuthally and with depth, is clearly the control volume (CV) formulation. As originally developed by Spalding and his students [e.g., *Patankar and Spalding*, 1972; *Patankar*, 1980] for engineering applications, this method has come to attract some attention in the area of planetary physics [e.g., *Ogawa et al*., 1991; *Tackley*, 1994, 1998; *Ratcliff et al*., 1996b; *Harder and Hansen*, 2005; *Stemmer et al*., 2006; *Tackley*, 2008] where applications have been presented in both Cartesian and spherical geometries. Even in the context of the atmospheric general circulation problem, especially when interactive chemistry is included, this methodology is gradually becoming strongly entrenched.

Our purpose in the present paper is to investigate the mantle mixing process and the degree of radial layering of the circulation to be expected in the presence of the deep-mantle perovskite-postperovskite (Pv-pPv)

exothermic phase transformation, transformational superplasticity (TS) [*Sauveur*, 1924; *Bachvar and Sviderskaya*, 1945; *Sammis and Dein*, 1974] at the 660 km depth of the endothermic phase transition, and the very recently identified second-order electronic spin transition in iron at midmantle depths [*Fyfe*, 1960; *Badro et al*., 2005; *Wu et al*., 2009] in mantle minerals that is now known to occur at midmantle pressures (60–70 GPa). To this end, we will employ a newly developed three-dimensional spherical control volume model, one that incorporates all of the important influences previously enumerated.

2. Mantle Transitions of Both Phase and Electronic Spin

Prior to presenting the methodology and the model results, we briefly review the most important pressure-temperature-induced transitions that are known to occur as a function of depth in the Earth's mantle.

2.1. Phase Transitions

The issue of the radial form of the convective circulation in Earth's interior is important to the understanding of mantle dynamical processes in both the deep Earth and at its surface. Beginning with the work of *Richter* [1973], the influence of mantle phase transitions upon the convection process has been extensively studied. In particular, the role of mantle phase transitions on the degree of mantle layering has been tested in a wide range of numerical models [*Christensen*, 1982; *Christensen and Yuen*, 1984, 1985; *Machetel and Weber*, 1991; *Peltier and Solheim*, 1992; *Solheim and Peltier*, 1993; *Tackley et al*., 1993; *Christensen*, 1995; *Brunet and Machetel*, 1998; *Shahnas and Peltier*, 2010]. At Earth-relevant conditions, an exothermic phase transition (in which the latent heat is released in transition from the low-pressure to high-pressure forms) energizes convective mixing, whereas an endothermic phase transition diminishes its strength. However, the degree of mantle layering that is expected to be due to the endothermic phase transition at 660 km depth has yet to be established definitively. A detailed recent review of the implications of high-resolution seismic tomographic imaging studies of several subduction zones has recently been provided by *Shahnas and Peltier* [2010], and no purpose will be served by repeating it here. Suffice it to say that in many such regions the downgoing slab is inferred to be either entirely arrested in its descent and lying flat across the endothermic horizon or accumulating within the transition zone between 420 and 660 km depth.

Based upon the earliest numerical work, the possibility of partial mantle layering [e.g., *Christensen and Yuen*, 1985; *Christensen*, 1995; *Machetel and Weber*, 1991; *Peltier and Solheim*, 1992; *Solheim and Peltier*, 1993; *Tackley et al*., 1993] due to the action of the endothermic transition was recognized. Temporary cold slab stagnation in the transition zone was later shown to be followed by a massive exchange of mass between the upper and lower mantle through the action of an avalanche process [*Peltier and Solheim*, 1992; *Brunet and Machetel*, 1998; *Tackley et al*., 1993]. This mechanism has been suggested to be the primary candidate for the explanation of the Wilson cycle of supercontinent creation and destruction [*Peltier et al*., 1997] and the generation of superplumes. The issue of the (effective) Clapeyron slope of the endothermic transition at 660 km depth continues to be an issue regarding the effectiveness of its impact upon convective mixing, the literature on which was also reviewed by *Shahnas and Peltier* [2010]. It is important to understand in this context that there in fact exists a series of phase transitions near the 660 km depth horizon involving the transformation of spinel + stishovite to ilmenite at ~20 GPa and from ilmenite to perovskite at ~24 GPa. The final transition in this sequence has a strongly negative Clapeyron slope (-6 ± 1 MPa/K). The net effect of the collectivity of these transitions at the base of the transition zone may therefore be extremely important.

2.2. Transformational Superplasticity

Large elongated structures in metals and alloys were first recognized by *Sauveur* [1924]; however, the term "superplasticity" was first employed by the Russian workers *Bachvar and Sviderskaya* [1945] to describe the creep regimes in which metal bars can undergo very large strains in tension without necking and was studied by *Pearson* [1934]. Based on many experimental observations, it is known that there is a mechanical weakening in some materials at the temperature where a change in crystal structure occurs, which can result in a large change in shape in pure metals under zero or very small stresses. The increased creep rate in some ceramics has also been observed by many workers [*Poirier*, 1985; *Maehara and Langdon*, 1990; *Meike*, 1993]. Transformational superplasticity may occur in some materials while there is a phase change occurring within them [*Sammis and Dein*, 1974]. Structural superplasticity refers to an extreme plasticity due to a strong reduction in the grain size after the transition is complete [*Rubie*, 1984]. Both types cause

an effective viscosity reduction in the material. Transformational superplasticity for which the effective viscosity of the material decreases due to continuous phase change has been studied and observed in metals, alloys, and ceramics; however, the possibility of superplastic deformation of nonmetallic materials such as mantle minerals under mantle conditions had not received much attention until *Sammis and Dein* [1974], two pioneers who attempted to measure the superplasticity of rocks and to extend the idea of superplasticity in the Earth's mantle through their experimental work on cesium chloride. The effectively aseismic nature of the lower mantle below 660 km depth may be attributed to the superplasticity of the mantle flow at the base of the transition zone where the mineral spinel dissociates to fine-grained composite of perovskite and magnesiowüstite with a eutectoid (mutual intergrowth) texture. The existence of a low-viscosity zone associated with the endothermic phase change at 660 km depth has been invoked in some global models of geoid anomalies [e.g., *Forte et al*., 1993; *Pari and Peltier*, 1995, 1996, 1998], glacial isostatic adjustment models [e.g., *Peltier*, 1998a, 1998b], and viscosity models derived from gravity data [*Soldati et al*., 2009]. Models of polar wander are also consistent with the viscosity models which include a thin, low-viscosity layer at the transition boundary [*Steinberger and O'Connell*, 1997]. Due to the reduction in viscosity across the phase transition, the Rayleigh number increases locally in this layer and the mantle flow becomes more dynamic and energetic which in turn may cause higher lateral variations in the temperature field and consequently higher lateral variations in the depth of the endothermic phase transition boundary. Since the endothermic transition-derived buoyancy forcing is proportional to the variation of the phase transition depth, under certain conditions, the presence of a superplastic layer may result to a higher degree of mantle layering. We will investigate this possibility in what follows.

2.3. A New "Transition" in Earth's Deep Mantle: The Electronic Spin Transition in Iron

The spin transition in iron from a high-spin (HS) state to a low-spin (LS) state with increasing pressure was first predicted by *Fyfe* [1960] but only supported as plausible on the basis of both crystal field theory [*Burns*, 1993; *Sherman*, 1988] and band theory [*Cohen et al*., 1997] to occur as a result of the compression of mantle material with increasing pressure. However, its existence has been experimentally confirmed only recently. The direct probing of the spin state of mantle minerals under high-pressure conditions only became possible as a consequence of the improvements in X-ray spectroscopy instruments on third-generation synchrotron sources combined with enhanced laser-heated diamond anvil cell technology [*Badro*, 2012], and the properties of mantle minerals could then be studied over the entire pressure and temperature range characteristic of Earth's mantle. The physical and chemical properties of iron-bearing minerals are quite different from those of iron-free minerals. This is because iron is a 3d transition metal with two stable valence states, Fe^{2+} and Fe^{3+}, with electronic configurations $[Ar]^{3d5}$ and $[Ar]^{3d6}$, respectively [*Badro et al*., 2005]. The LS state of iron is expected to have a smaller ionic radius than its HS counterpart [*Shannon and Prewitt*, 1969], and due to an decrease in the number of unpaired 3d electrons in the LS state, the magnetic susceptibility of the mineral decreases in the HS-LS crossover [*Burns*, 1993]. This change in spin state is expected to influence all of the physical properties of mantle minerals and consequently the style of the convective mixing process [*Lin et al*., 2008; *Wentzcovitch et al*., 2009; *Wu et al*., 2009; *Wu and Wentzcovitch*, 2014] and consequently is expected to influence the style of mantle convection.

Based on high-pressure experiments, the HS-LS crossover in iron is now known to occur in the range of pressure from 60 to 70 GPa in ferropericlase $(Mg_{0.83}Fe_{0.17})O$ [*Badro et al*., 2003]. High-resolution Kβ X-ray spectroscopy has revealed that the iron in ferropericlase is entirely in the LS state at pressures greater than 75 GPa [*Badro et al*., 2003]. Despite the fact that LS minerals have higher density than their HS counterparts (due to the smaller molar volume of LS minerals because of the impact of pressure), the HS-LS transition could be seismically transparent and the crossover-related anomalies in radial seismic velocity profiles in a pyrolitic lower mantle could be subtle with no obvious signature [*Cammarano et al*., 2010; *Badro*, 2012; *Wu et al*., 2013; *Wu and Wentzcovitch*, 2014]. Based on inelastic X-ray scattering measurements on $(Mg_{0.83}Fe_{0.17})O$ ferropericlase, *Antonangeli et al*. [2011] reported that spin transition effects on the elastic properties are limited to only the shear moduli of the elastic tensor, which may explain the lack of a one-dimensional seismic signature of the spin crossover. However, in the most recent report of *Badro* [2012], a possible seismic transparency of the spin transition is suggested to be related to the consistent increase in both density and adiabatic bulk modulus such that the seismic parameter, K/ρ, remains unchanged. Despite the lack of radial signature, the lateral heterogeneities in bulk and longitudinal velocities ($V_\phi = \sqrt{K/\rho}$ and $V_p = \sqrt{(K + 4\mu/3)/\rho}$, respectively) are robust [*Wu and Wentzcovitch*, 2014].

The recent work of *Wu and Wentzcovitch* [2014] based on density functional theory computational methods suggests in fact that the spin change in iron in ferropericlase may also offer an alternative interpretation for the observed seismic velocity anomalies at midmantle depths usually interpreted to imply compositional heterogeneity [e.g., *Ishii and Tromp*, 1999]. Their first-principle calculations reveal an anticorrelation between shear and bulk sound velocities ($V_s = \sqrt{\mu/\rho}$ and $V_\phi = \sqrt{K/\rho}$, respectively) in homogeneous aggregates containing ferropericlase [*Wu and Wentzcovitch*, 2014]. The spin crossover can also suppress thermally induced heterogeneity in longitudinal velocity (V_p) at certain depths without significant impact in shear velocity (V_s).

The HS-LS transition in ferropericlase may also increase the partition coefficient of iron between ferropericlase and magnesium silicate perovskite by several orders of magnitude [*Badro et al*., 2003], depleting the perovskite phase of its iron. This may cause stratification in the lower mantle with a phase mixture of approximately equal partitioning of iron between magnesium silicate perovskite and ferropericlase in the upper layer and a mixture of almost iron-free perovskite and iron-rich ferropericlase in the lower layer [*Badro et al*., 2003]. The melting point of an iron-free perovskite is significantly higher than its iron-bearing counterpart [*van Keken et al*., 1995; *Zerr and Boehler*, 1993], and in many minerals, the viscosity increases with the increase of the melting temperature [*Weertman and Weertman*, 1975], and therefore, perovskite, as the major constituent mineral of the lower mantle, will have higher viscosity in the lower regions of the mantle [*Badro et al*., 2003; *Badro*, 2012]. Although the importance of the spin transition in ferropericlase is well established, debate continues concerning its possible importance in the more abundant perovskite phase, a debate that has also been reviewed by *Shahnas et al*. [2011].

In the new model of the mantle convection process that is fully developed in what follows, our goal is to incorporate all of the above physical characteristics in an isochemical framework. We view this as potentially important as the work of *Wu and Wentzcovitch* [2014] suggests that the seismic transition at midlower mantle depths, which has been commonly interpreted as implying compositional stratification, may simply be a consequence of the occurrence of the spin transition in iron. If this were the case, it would demand an important revision of the currently prevailing view that the mantle convection process is fundamentally thermocompositional in nature rather than essentially isochemical. In our analysis of this issue below, which extends those discussed in terms of axisymmetric convection models in an earlier paper [*Shahnas et al*., 2011], we will explore the consequences in terms of the expected nature of the heterogeneities that would be caused by the modulation of the convective circulation by the influence of the spin transition.

3. A Control Volume Formulation for Multiphase Mantle Convection

3.1. Yin-Yang Grid

The standard form of the Yin-Yang grid is an overset grid formed by two geometrically identical grids as described by *Kageyama and Sato* [2004] in detail. This grid, which is illustrated in Figures 1a–1c, consists of two latitude-longitude (θ-ϕ) grids each with $\pm 45 \pm \delta°$ ($\delta \sim \Delta\vartheta$) latitudinal domain covering 270° of longitude which taken together tile the sphere in a way that is entirely analogous to the covering of a tennis ball. The two patches (Yin and Yang) are both covered in their interiors by orthogonal coordinates and are symmetrical so that similar routines may be used in solving the conservation equations that are employed to describe the mantle convection process. However, unlike the icosahedral or cubed sphere grids, the Yin and Yang grids do not connect in a simple fashion so that interpolation schemes are required at the overlapping boundaries to accurately connect them. The overlap area required to accomplish this is approximately 6% of the surface area of the sphere and could be further reduced by employing a modified version of Yin-Yang grid with curved boundaries instead of quasirectangular boundaries [*Kageyama and Sato*, 2004]. Some modified versions of Yin-Yang overlapping grids such as the three identical-patch grid [*Kageyama and Sato*, 2004] or the extended Yin (i.e., cover the full Yin grid) with two reduced Yang grids or Yang caps [*Staniforth and Thuburn*, 2012] have also been proposed. In our model calculations, we employ a modified form of the standard Yin-Yang grid in which the Yin and Yang components are both extended (full in the longitudinal extent of the domain). This increases the computational load by approximately 25% but reduces the boundary overlap and has proven to be much more capable of preserving symmetry. The fields in the regions of overlap of the Yin and Yang grids are averaged. The boundary values at the edges across which the Yin and Yang grids must be connected in our calculations are obtained by bicubic Lagrange interpolation [e.g., *Li et al*., 2006] using the internal grid points of the two patches of the tiling (see Figures 1d–1f).

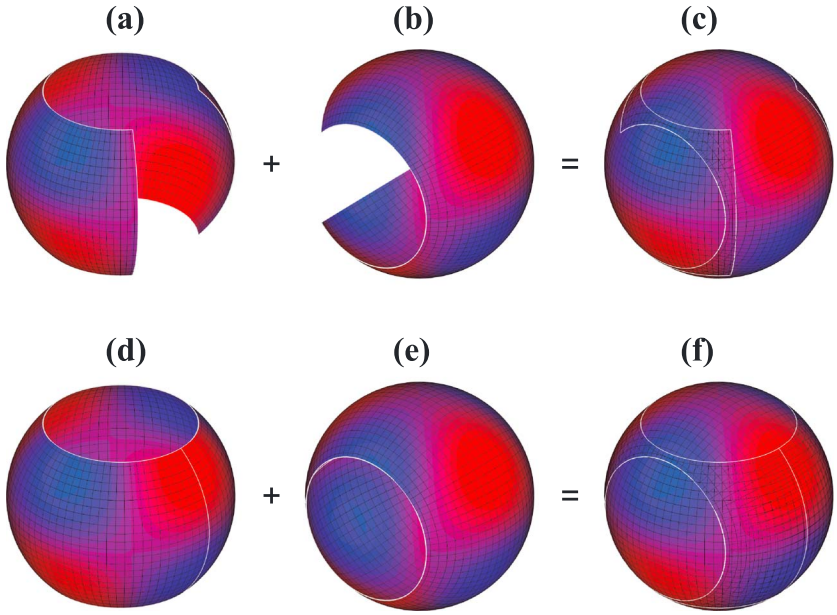

Figure 1. (a) Yin grid, (b) Yang grid, (c) combined Yin-Yang grid, (d) modified Yin grid, (e) modified Yang grid, (f) modified Yin and Yang grids combined to cover a spherical sphere with extended overlap employed in this study.

3.2. Thermomechanical Equations

The anelastically compressible mantle convection model documented herein is based upon the application of the control volume method to solve the basic hydrodynamic equations at high Prandtl number where the inertial forces are negligible in a three-dimensional spherical shell. The set of nonlinear partial differential equations that define the model consists of conservation equations for mass (continuity), momentum, and internal energy. This set of simultaneous equations is solved in the anelastic approximation by which we mean that compressibility is incorporated solely in the background hydrostatically balanced variation of density of the medium within which the convection process occurs so that the local time derivative of the density field required to support the propagation of sound waves is eliminated from the conservation of mass relation. The equation of state for the convecting medium, for application to the Earth, will be assumed to include the important olivine-spinel and spinel-perovskite + magnesiowüstite phase transitions at 410 km and 660 km depths, respectively, as well as the deep-mantle perovskite-postperovskite (Pv-pPv) phase transition at approximately 2700 km depth discovered by *Murakami et al.* [2004] on the basis of high-pressure mineral physics experiments. The final model for which results will be provided in section 6 will be for the influence of the HS-LS spin transition in iron. The anelastic form of the continuity equation on which the model is based is simply

$$\nabla \cdot \left(\overline{\rho}\vec{V}\right) = 0, \tag{1}$$

in which the variable $\overline{\rho}$ is the hydrostatically balanced depth-dependent density field of the background state.

In the infinite Prandtl number approximation in which the inertial force may be neglected relative to the viscous force, the expression for conservation of momentum is

$$-\nabla P + \nabla \cdot \overline{\overline{\sigma}} - \rho g \hat{r} = 0, \tag{2}$$

where the deviatoric stress tensor is given by

$$\overline{\overline{\sigma}} = \eta\left[\nabla\vec{V} + \left(\nabla\vec{V}\right)^T\right] - \frac{2}{3}\eta\left(\nabla\cdot\vec{V}\right)\overline{\overline{I}}. \tag{3}$$

The partial differential equation describing the conservation of internal energy, on the other hand, is

$$C_p\overline{\rho}\,\frac{DT}{Dt} - \alpha T\,\frac{DP}{Dt} = \nabla\cdot(k\nabla T) + \Phi + \overline{\rho}H + \overline{\rho}l_i\frac{D\Gamma_i}{Dt}. \tag{4}$$

The final relation required in order to close the system of partial differential equations of the model is the equation of state, which may be written for our purposes in the approximate form:

$$\rho = \overline{\rho}\left[1 - \alpha(T - T_r) + \frac{1}{K_T}(P - P_r)\right] + \Delta\rho_i(\Gamma_i - \Gamma_{ri}), \qquad i = 1, 2, 3. \tag{5}$$

In this system of equations, $\overline{\rho}$, ρ, g, α, T, T_r, $\vec{V}$, P, P_r, H, Φ, η, C_P, k, K_T, t, and $\hat{r}$ denote the background radial variation of density due to the self-compression of mantle material, total density, gravitational acceleration, thermal expansion coefficient, temperature, reference temperature, velocity, pressure, reference pressure, internal heating rate, viscous energy dissipation rate, molecular viscosity in shear, heat capacity at constant pressure, thermal conductivity, bulk modulus at constant temperature, time, and the unit vector in the radial direction, respectively.

The quantities l_i in equation (4) and $\Delta\rho_i$ in equation (5) represent the latent heat of transformation and the density contrast between two solid phases across divariant phase transition i, and Γ_i is a phase density functional defined by [e.g., *Richter*, 1973]

$$\Gamma_i = \frac{1}{2}[1 + \tanh(\pi_i)], \tag{6}$$

where the nondimensional arguments of the hyperbolic tangent functions are given by

$$\pi_i = \frac{d_i - d - \gamma_i(T - T_i)}{h_i}. \tag{7}$$

In equation (7), the parameters d, d_i, h_i, T_i, and γ_i are depth, reference depth of phase boundary i, width of the ith divariant phase transition, transition temperature at the reference depth d_i, and the Clapeyron slope of the relevant phase transition, respectively. The important viscous dissipation rate of energy per unit volume of the mantle in equation (4) in three-dimensional spherical geometry has the following explicit form [e.g., *Winter*, 1977] in each of the Yin and Yang patches:

$$\begin{aligned}\Phi = 2\eta\left\{\left[\frac{\partial V_r}{\partial r}\right]^2 + \left[\frac{1}{r}\frac{\partial V_\theta}{\partial\theta} + \frac{V_r}{r}\right]^2 + \left[\frac{1}{r\sin(\theta)}\frac{\partial V_\phi}{\partial\phi} + \frac{V_r}{r} + \frac{V_\theta\cot(\theta)}{r}\right]^2 - \frac{1}{3}\left[\nabla\cdot\vec{V}\right]^2\right\} \\ + \eta\left[\frac{\partial V_\theta}{\partial r} - \frac{V_\theta}{r} + \frac{1}{r}\frac{\partial V_r}{\partial\theta}\right]^2 + \eta\left[\frac{\sin(\theta)}{r}\frac{\partial}{\partial\theta}\left(\frac{V_\phi}{\sin(\theta)}\right) + \frac{1}{r\sin(\theta)}\frac{\partial V_\theta}{\partial\phi}\right]^2 \\ + \eta\left[\frac{1}{r\sin(\theta)}\frac{\partial V_r}{\partial\phi} + r\frac{\partial}{\partial r}\left(\frac{V_\phi}{r}\right)\right]^2.\end{aligned} \tag{8}$$

We employ the following scheme to nondimensionalize the governing field equations:

$$\begin{aligned} &r = r'\Delta r, \qquad T = T'\Delta T, \quad \eta = \eta'\eta_0, \quad k = k'k_0, \quad \rho = \rho'\rho_0, \quad C_P = C_P'C_0, \\ &g = g'g_0, \quad \alpha = \alpha'\alpha_0, \quad \kappa = \kappa'\kappa_0, \qquad t = t'\frac{d^2}{\kappa_0}, \quad P = P'\frac{\eta\kappa_0}{d^2}, \quad \sigma = \sigma'\frac{\eta\kappa_0}{d^2}, \end{aligned} \tag{9}$$

in which zero-subscripted quantities denote a reference value of the parameter and κ is the thermal diffusivity. As characteristic length and temperature scales, we employ, respectively, $\Delta r = R_{\text{surf}} - R_{\text{CMB}}$ and $\Delta T = T_{\text{CMB}} - T_{\text{surf}}$.

The nondimensional momentum equation is then given by

$$-\nabla' P' + \nabla'\cdot\overline{\overline{\sigma}}' - R_0\rho' g'\hat{r} = 0, \tag{10}$$

where the Rayleigh number of the system is

$$R_0 = \frac{g_0\rho_0 d^3}{\eta_0\kappa_0}. \tag{11}$$

Dropping the primes in order to simplify the notation then reduces equation (10) to

$$-\nabla P + \nabla\cdot\overline{\overline{\sigma}} - R_0\rho g\hat{r} = 0. \tag{12}$$

The components of the momentum equations and the stress tensors in spherical geometry are given in Appendix A. The nondimensional form of the energy equation may be written [*Shahnas and Peltier*, 2010] as

$$(C_P - \alpha_i l_i)\left(\frac{\partial}{\partial t}(\overline{\rho}T) + \nabla\cdot\left(\overline{\rho}T\vec{V}\right)\right) + \xi_0\alpha T V_r\overline{\rho}g = \nabla\cdot(k\nabla T) + \delta_0\Phi + \gamma_0\overline{\rho}H + \omega_0\overline{\rho}\beta_i l_i, \tag{13}$$

Table 1. Comparison of the Mean Temperatures, Nusselt Numbers, and RMS Velocities for the Models With Tetrahedral Symmetry at $Ra_{1/2} = 7 \times 10^3$ on $2 \times \theta \times \phi \times r = 2 \times 70 \times 240 \times 49$ Grid[a]

Model	$Ra_{1/2}$	$\Delta\eta$	$<T>$	$<Nu_t>$	$<Nu_b>$	$<V_{RMS}>$
T01	7×10^3	1	0.2287	3.5549	3.5204	31.57
Zh			0.217	3.5126	3.4919	32.66
YK				3.4430		32.08
Rt				3.4423		32.19
Iw				3.45		32.41
TS				3.6565		32.93
Ka			0.2159	3.4945		32.63
Ta				3.48		32.57
St				3.4864	4.4864	32.58
T02	7×10^3	10	0.2484	3.2722	3.2385	25.96
Zh			0.236	3.2674	3.2491	27.36
Ka			0.23469	3.2482		27.28
St				3.2398	3.2399	27.25
T03	7×10^3	20	0.2553	3.1722	3.1333	24.58
Zh			0.243	3.1724	3.1548	25.85
YK				3.1330		26.10
Rt				3.1615		25.69
Ka			0.2418	3.1534		25.76
Ta				3.15		25.71
St				3.1447	3.1450	25.73
T04	7×10^3	10^2	0.2792	2.9290	2.8908	22.62
Zh			0.265	2.9354	2.9205	23.11
T05	7×10^3	10^3	0.3269	2.5239	2.5196	22.24
Zh			0.312	2.5468	2.5352	22.90

[a]T01–T05 represent our model results with tetrahedral symmetry. The abbreviation code names "Zh" stands for *Zhong et al.* [2008], "YK" for *Yoshida and Kageyama* [2004], "Rt" for *Ratcliff et al.* [1996a], "Iw" for *Iwase* [1996], "TS" for *Tabata and Suzuki* [2000], "Ka" for *Kameyama et al.* [2008], "Ta" for *Tackley* [2008], and "St" for *Stemmer et al.* [2006].

where the further nondimensional parameters appear as

$$\xi_0 = \frac{\alpha_0 g_0 d}{C_0}, \quad \delta_0 = \frac{\eta_0 \kappa_0}{C_0 \rho_0 \Delta T d^2}, \quad \gamma_0 = \frac{H_0 d^2}{C_0 \kappa_0 \Delta T}, \quad \omega_0 = \frac{\eta_0 \kappa_0}{d^2 C_0 \rho_0 \Delta T}. \tag{14}$$

A power law advection scheme [*Patankar*, 1980; *Shahnas and Peltier*, 2010] has been employed in our control volume formulation. The solution of the discretized equations is obtained using the tridiagonal matrix algorithm described by *Patankar* [1980]. The momentum and energy equations are integrated over Δv and $\Delta v \Delta t$, respectively [*Patankar*, 1980; *Shahnas and Peltier*, 2010], where Δv is the spherical control volume element and Δt is the time step. A staggered grid [*Harlow and Welch*, 1965] in which the pressure is defined in the center of each cell and velocity components are defined at cell boundaries has been employed. Employing the message passing interface, the solution of the system of thermomechanical equations is parallelized by dividing the three-dimensional spherical shell domain (with lateral extents $\theta = \pm 45 \pm \delta°$) of the Yin and Yang patches into a number of "slices," each of which itself consists of a number of latitude-depth planes.

4. Initial Benchmark Tests of the Yin-Yang Control Volume-Based Model

Prior to applying it to the complex problems for the Earth which will be our ultimate focus, the code has been tested extensively against previously published benchmark results. The general form of the thermal perturbation superimposed on a conduction solution to describe the initial conditions for a given model run in these benchmark tests is expressed as

$$T(r, \theta, \phi) = \frac{r_b (r - r_t)}{r (r_b - r_t)} + \sum_m \left[\varepsilon_{cm} \cos(m\phi) p_{lm}(\theta) + \varepsilon_{sm} \sin(m\varphi) p_{lm}(\theta) \right] \sin\left[\frac{\pi (r - r_b)}{(r_t - r_b)} \right], \tag{15}$$

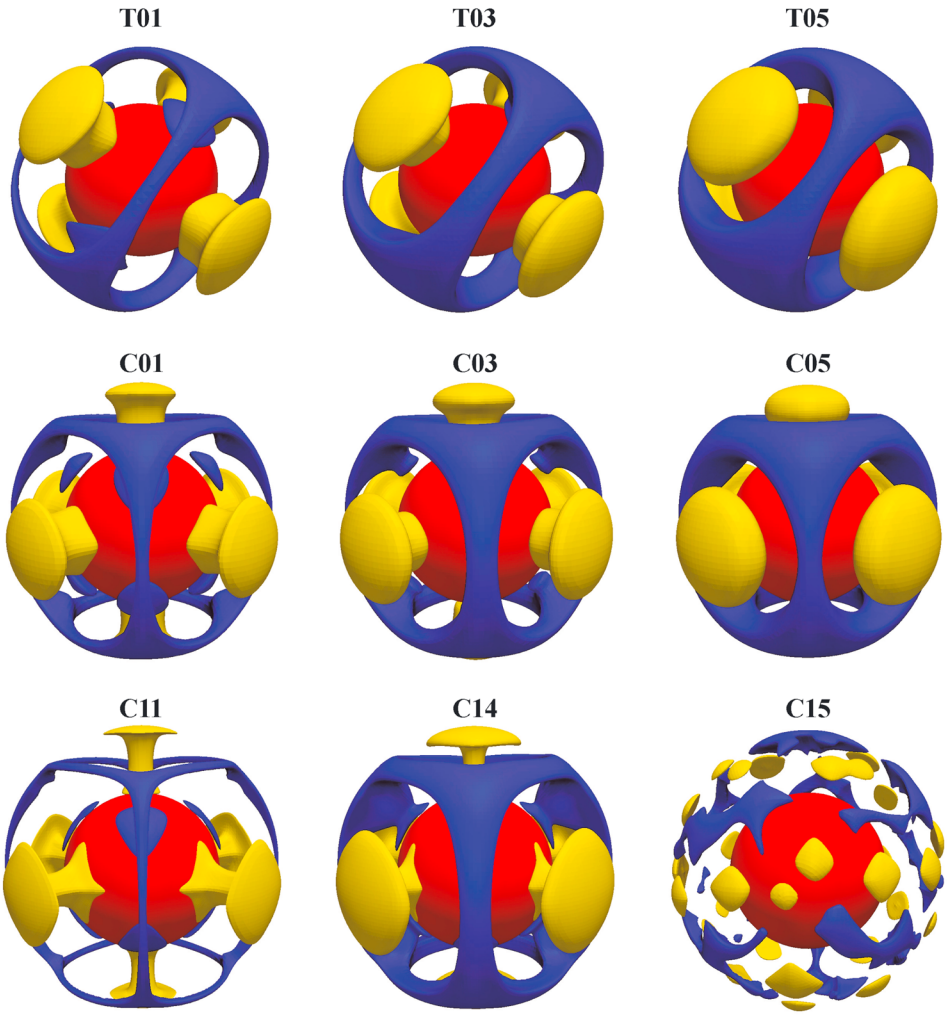

Figure 2. Benchmark test models: T01, T03, and T05 are models with tetrahedral symmetry at $Ra_{1/2} = 7 \times 10^3$ and $\Delta\eta = 1$, 20, and 10^3, respectively; C01, C03, and C05 are models with cubic symmetry at $Ra_{1/2} = 7 \times 10^3$ and $\Delta\eta = 1$, 30, and 10^3, respectively; C11, C14, and C15 are models with cubic symmetry at $Ra_{1/2} = 10^5$ and $\Delta\eta = 1$, 10^3, and 10^6, respectively.

where l and m are the spherical harmonic degree and order, respectively; ε_{cm} and ε_{sm} are the magnitudes of the individual spherical harmonic constituents; and p_{lm} is the normalized associated Legendre polynomial given by

$$p_{lm}(\theta) = \sqrt{\frac{(2l+1)(l-m)!}{2\pi(1+\delta_{m0})(l+m)}}\,\overline{p}_{lm}(\theta). \tag{16}$$

The curvature defined as the ratio of the radii of the inner and outer bounding surfaces of the spherical shell ($f = R_{\text{bot}}/R_{\text{surf}}$) in our numerical models is 0.547 (Earth-like curvature). For tetrahedral symmetry, the harmonic degree and order of the initial temperature perturbation are $l = 3$ and $m = 2$, respectively, and $\varepsilon_{c2} = \varepsilon_{s2} = 0.01$. For cubic symmetry, we assume $l = 4$ and $m = 0 + 4$ with the magnitudes of $\varepsilon_{c0} = \varepsilon_{s0} = 0.01$ and $\varepsilon_{c4} = \varepsilon_{s4} = 0.01 \times 7/5$ [*Zhong et al.*, 2008]. In the case of test models with variable viscosity, a temperature-dependent viscosity of the form

$$\eta(T) = A \exp[E(T_{\text{ref}} - T)] \tag{17}$$

is assumed in which T_{ref} is the reference temperature for the viscosity ($T_{\text{ref}} = \Delta T/2 + T_{\text{surf}}$) and the activation energy parameter ($E = \ln(\Delta\eta)$) controls the viscosity variation within the shell. Therefore, the viscosity achieves its maximum (minimum) at the top surface (core-mantle boundary surface).

Table 2. Comparison of the Mean Temperatures, Nusselt Numbers, and RMS Velocities for the Models With Cubic Symmetry at $Ra_{1/2} = 7 \times 10^3$ on $2 \times \theta \times \phi \times r = 2 \times 70 \times 240 \times 49$ Grid[a]

Model	$<Ra_{1/2}>$	$\Delta\eta$	$<T>$	$<Nu_t>$	$<Nu_b>$	$<V_{RMS}>$
C01	7×10^3	1	0.2249	3.5931	3.6069	30.36
Zh			0.217	3.6254	3.6016	31.09
YK				3.5554		30.51
Rt				3.5806		30.87
Ka			0.2163	3.6083		31.07
St				3.5982	3.5984	31.02
C02	7×10^3	20	0.2622	3.3194	3.3280	24.35
Zh			0.252	3.3721	3.3513	25.13
YK				3.3280		25.38
Rt				3.3663		25.17
Ka			0.2511	3.3525		25.06
St				3.3423	3.3427	25.98
C03	7×10^3	30	0.2686	3.2676	3.2750	23.68
Zh			0.258	3.3162	3.2960	24.35
Ka			0.2572	3.2969		24.24
St			3.2864	3.2869		24.19
C04	7×10^3	10^2	0.2910	3.0859	3.1012	22.38
Zh			0.279	3.1278	3.1093	22.49
C05	7×10^3	10^3	0.3417	2.6493	2.6982	22.26
Zh_B5			0.330	2.6780	2.6635	22.29
Ka			0.274	7.04	7.04	
C06	7×10^3	10^7	0.5886	3.4336	3.6206	157.72
Zh			0.589	3.4753	3.5171	158.7

[a]C01–C06 represent our model results with cubic symmetry. The abbreviation code names "Zh" stands for *Zhong et al.* [2008], "YK" for *Yoshida and Kageyama* [2004], "Rt" for *Ratcliff et al.* [1996a],"Ka" for *Kameyama et al.* [2008], and "St" for *Stemmer et al.* [2006].

Our numerical results for the Nusselt numbers at the upper and lower boundaries of the shell, mean temperatures, and mean RMS velocities for the models with temperature-dependent viscosity ranging from $\Delta\eta = 1$ to $\Delta\eta = 10^3$ ($\Delta\eta = \exp(E)$) at $Ra_{1/2} = 7 \times 10^3$ are presented in Table 1 for the models with initial tetrahedral perturbation symmetry. $Ra_{1/2}$ is defined by the reference viscosity η_{ref} (T_{ref}) [*Ratcliff et al.*, 1996a]. T01, T03, and T05 in Figure 2 display the steady states for this symmetry with four upwelling plumes at different viscosity contrasts. The results are compared with published benchmark results for these cases in Table 1. The statistical data for the models with cubic perturbation symmetry are listed in Table 2 where they are also compared with the

Table 3. Comparison of the Mean Temperatures, Nusselt Numbers, and RMS Velocities for the Models With Cubic Symmetry at $Ra_{1/2} = 10^5$ on $2 \times \theta \times \phi \times r = 2 \times 70 \times 240 \times 65$ Grid[a]

Model	$Ra_{1/2}$	$\Delta\eta$	$<T>$	$<Nu_t>$	$<Nu_b>$	$<V_{RMS}>$
C11	10^5	1	0.1955	7.6488	7.6656	145.50
Zh-C1			0.1728	7.8495	7.7701	154.8
St-Case1[b]			0.1941	7.3717	7.3721	153.13
Ta				7.27		160.2
C12	10^5	30	0.2206	6.6817	6.6879	109.03
Zh-C3			0.2011	6.7572	6.7182	109.1
C13	10^5	100	0.2372	6.4132	6.4300	99,26
Zh-C4			0.2168	6.4803	6.4362	98.90
C14	10^5	10^3	0.3201	6.1576	6.2006	97.18
St-Case4[b]			0.3335	6.0791	6.0893	88.14
Ta				6.06		96.8
C15	10^5	10^6	0.6436	5.8593	6.1716	446.25
St-Case7[b]			0.6530	6.0859	6.0851	416.50
Ta				6.50		404

[a]C11–C15 represent our model results with cubic symmetry. The abbreviation code name "Zh" stands for *Zhong et al.* [2008], "St" for *Stemmer et al.* [2006], and "Ta" for *Tackley* [2008].
[b]Started from random perturbations of small wavelength.

available benchmark results. The models C01, C03, and C05 displayed in Figure 2 represent steady states for the cubic symmetry with six upwelling plumes. C06 is in a so-called stagnant lid regime with many small plumes at depth [*Zhong et al*., 2008; *Tackley*, 1993; *Ratcliff et al*., 1996a, 1996b]. The results at $Ra_{1/2} = 7 \times 10^5$ for cubic symmetry are listed in Table 3 where they are compared with the benchmark results of *Stemmer et al*. [2006], *Zhong et al*. [2008], and *Tackley* [2008]. Our model results for the model C11 at $Ra_{1/2} = 7 \times 10^5$ (Table 3) are more consistent with the model results of *Zhong et al*. [2008] due perhaps to the fact that in both models the cubic symmetry is preserved. The results demonstrate that even in this isoviscous model at $Ra_{1/2} = 7 \times 10^5$ the symmetry of the upwelling plumes and downwelling cold material is preserved. Despite an ~5% energy nonconservation in model C15 with the viscosity contrast of 10^6 at $Ra_{1/2} = 7 \times 10^5$ (which could be improved by employing a more sophisticated solver), Tables 1–3 demonstrate the power of our code in solving both uniform and strongly variable viscosity convection problems. Our model results agree well with the published benchmark results within a few percent or better, further confirming the validity of our code.

5. The Control Volume-Based Formulation Applied to a Model of the Earth

In this section, we will present the physical properties formulations to be employed in our control volume-based Earth models in which mineral properties are strong functions of position due either to explicit or implicit dependence upon temperature and pressure. A recent review of our understanding of the high-pressure mineral physics and heterogeneity of the mantle will be found in *Stixrude and Lithgow-Bertelloni* [2012]. Employing 3-D spherical control volume models, an interest in this initial study is to estimate the extent to which the influence of the pressure-induced mantle phase transitions may have been exaggerated by the use of axisymmetric spherical models in our previous work [*Shahnas and Peltier*, 2010], and therefore, in these new 3-D spherical control volume models, we will employ the same mantle parameters as were employed previously in their axisymmetric counterparts. We will then proceed to investigate the impact of transformational superplasticity [*Bachvar and Sviderskaya*, 1945] at the endothermic phase transition level on the degree of mantle layering. In our final model, we will investigate the combined impact of solid-solid phase transitions, transformational superplasticity at the endothermic phase transition level, a low viscosity in D″, and finally the influence of the high-spin to low-spin (HS-LS) crossover in iron occurring in the ferropericlase phase of the mantle material [*Badro et al*., 2003] at lower mantle pressures on the style of mantle convection. This final model will also include the influence of a 50 km thick approximation to the lithosphere at the Earth's surface (this should be understood to represent a sensitivity test of the impact of reduced surface mobility upon surface heat flow rather than an attempt to represent the realistic influence of the variable thickness of the elastic surface lithosphere) [e.g., *Peltier*, 1986, 1988]. Prior to presenting the model results, it will be useful to describe the specific representations to be employed for the most important physical properties that control the dynamics and radial heat transfer of the convection process within the spherical shell.

5.1. Thermal Expansivity

In applying the numerical method to the Earth, we will employ a pressure- and temperature-dependent thermal expansivity. It may be described as [e.g., *Fei*, 1995]

$$\alpha(P,T) = \alpha_0(T)\left(\frac{v(P,T)}{v(0,T)}\right)^{\delta_T}, \tag{18}$$

where δ_T is the Anderson-Gruneisen parameter and v is the volume at pressure P and temperature T. We calculate the thermal expansion coefficient from equation (18) by incorporating the third-order Birch-Murnaghan equation of state [e.g., *Schmeling et al*., 2003] as

$$P = 3C(1+2C)^{5/2}K_{T_0}(T)\left[1 - \frac{3}{2}\left(4 - K'_{T_0}\right)C\right], \tag{19}$$

where $K_{T_0}(T)$ is the isothermal bulk modulus at zero pressure, K'_{T_o} is its pressure derivative, and the compression C is given by

$$C = \frac{1}{2}\left[\left(\frac{V(0,T)}{V(p,T)}\right)^{2/3} - 1\right]. \tag{20}$$

$K'_{T_0} = 5.37$ [*Fei*, 1995; *Schmeling et al*., 2003] will be assumed throughout what follows.

As in *Shahnas and Peltier* [2010], we continue to employ a power law relation for the temperature-dependent part of this coefficient [*Fei*, 1995] as

$$\alpha_0(T) = a_0 + a_1 T + a_2 T^{-2}. \tag{21}$$

For forsterite, the parameters in (21) are given by *Fei* [1995] as

$$a_0 = 3.034 \times 10^{-5}\ \mathrm{K}^{-1}, \quad a_1 = 7.422 \times 10^{-9}\ \mathrm{K}^{-2}, \quad a_2 = -0.5381\ \mathrm{K}.$$

To obtain the bulk modulus temperature dependence, we employ the isothermal Anderson-Gruneisen parameter δ_T as

$$\delta_T = -\frac{1}{\alpha K_T}\left(\frac{\mathrm{d}K_T}{\mathrm{d}T}\right)_P. \tag{22}$$

Above the Debye temperature, δ_T and αK_T may be assumed to be temperature independent. Subject to this approximation, equation (22) may be integrated [*Kumar*, 2000] to obtain

$$K_{T0}(T) = K_0\left[1 - \alpha_0 \delta_T^0 (T - T_0)\right]. \tag{23}$$

The parameters for the mantle mineral Forsterite are, again given by *Fei* [1995], as

$$K_0 = 129\ \mathrm{GPa}, \quad \alpha_0 = 2.64 \times 10^{-5}\ \mathrm{K}^{-1}, \quad \delta_T^0 = 5.5, \quad T_0 = 298\ \mathrm{K}.$$

The thermal expansivity is assumed to be bounded above by the value $3.0 \times 10^{-5}\,\mathrm{K}^{-1}$ near the surface of the convecting region.

5.2. Thermal Conductivity

Also, in application of the model to the Earth, the pressure- and temperature-dependent form of the thermal conductivity proposed by *Hofmeister* [1999] will be employed as

$$k(P,T) = k(298)\left(\frac{298}{T}\right)^a \exp\left[-\left(4\gamma + \frac{1}{3}\right)\int_{298}^{T}\alpha(\theta)\mathrm{d}\theta\right]\left(1 + \frac{K_0'}{K_0}\right) + \sum_0^3 b_i T^i. \tag{24}$$

The two terms in this semiempirical relation are respectively the lattice vibration (phonon) and radiative transport (photon) contributions. The parameters in this equation [*Hofmeister*, 1999; *van den Berg et al.*, 2002] are

$$k(298) = 4.7\ \ \mathrm{W\,m^{-1}\,K^{-1}}, \quad a = 0.3, \quad \gamma = 1.2\ \mathrm{K}, \quad K_0' = 4\ \mathrm{GPa}, \quad K_0 = 261\ \mathrm{GPa},$$
$$b_0 = 1.7530 \times 10^{-2}, \quad b_1 = -1.0365 \times 10^{-4}, \quad b_2 = 2.2451 \times 10^{-7}, \quad b_3 = -3.4071 \times 10^{-11}.$$

The thermal conductivity has been assumed to be bounded below by the value $2.5\,\mathrm{W\,m^{-1}\,K^{-1}}$ near the surface.

5.3. Viscosity

In our numerical Earth models, we assume a VM3 depth-dependent viscosity profile based upon constraints provided by the process of glacial isostatic adjustment [*Peltier*, 1998b; *Peltier and Drummond*, 2010] and so, for the purpose of these initial analyses, we will be ignoring the influence of lateral viscosity heterogeneity. Modified versions of VM3 which include a low-viscosity layer at the endothermic phase transition depth (representing superplasticity at this depth), a low-viscosity D″ layer, and a lithosphere of moderate viscosity to mimic the influence of sluggish surface dynamics will be used in our final Earth models.

6. Results

The sequence of Earth models to be analyzed and compared with their axisymmetric counterparts consists of three models denoted E000, E110, and E111, respectively, with no phase transitions, with two phase transitions at 410 km and 660 km depths, and with three phase transitions at 410 km, 660 km, and 2700 km depths. The thermal expansivity and thermal conductivity employed in these models are both pressure and temperature dependent [*Fei*, 1995; *Schmeling et al.*, 2003; *Hofmeister*, 1999] with the depth-dependent VM3 viscosity profile [*Peltier*, 1998b] as described in sections 5.1. Figure 3 displays the VM3 viscosity profile and the depth variation of the thermal expansivity and thermal conductivity for a sample geotherm (Figure 3b). The thermal history

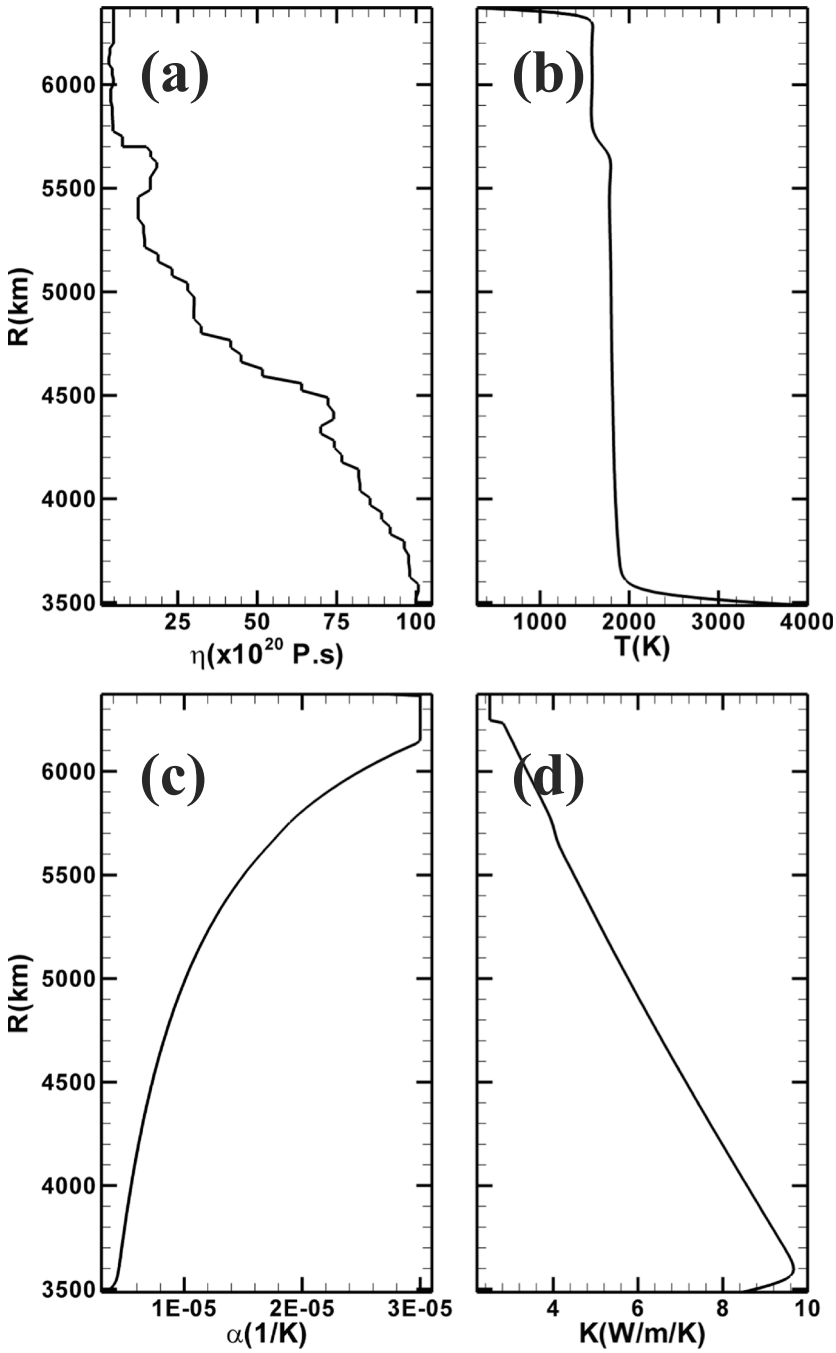

Figure 3. (a) VM3 viscosity profile [*Peltier*, 1998b; *Peltier and Drummond*, 2010], (b) a sample geotherm, (c) temperature- and pressure-dependent thermal expansivity [*Schmeling et al*., 2003] with an upper limit of $3.0 \times 10^{-5}\,K^{-1}$ near the surface, and (d) temperature- and pressure-dependent thermal conductivity [*Hofmeister*, 1999] with a lower limit of $2.5\,W\,m^{-1}\,K^{-1}$ near the surface.

Table 4. Time-Averaged Mantle Mean Temperature and Surface Heat Flux of the Axisymmetric Spherical Models [*Shahnas and Peltier*, 2010] Are Compared With Similar Quantities of the 3-D Spherical Models Discussed in This Paper

Axisymmetric Spherical Models	*T* (K)	HF_{surf} (TW)	3-D Spherical Models	T (K)	HF_{surf} (TW)
C00D00VM3	1607	51.0	E110	1572	53.6
C12D80VM3	1755	59.4	E111	1748	63.7

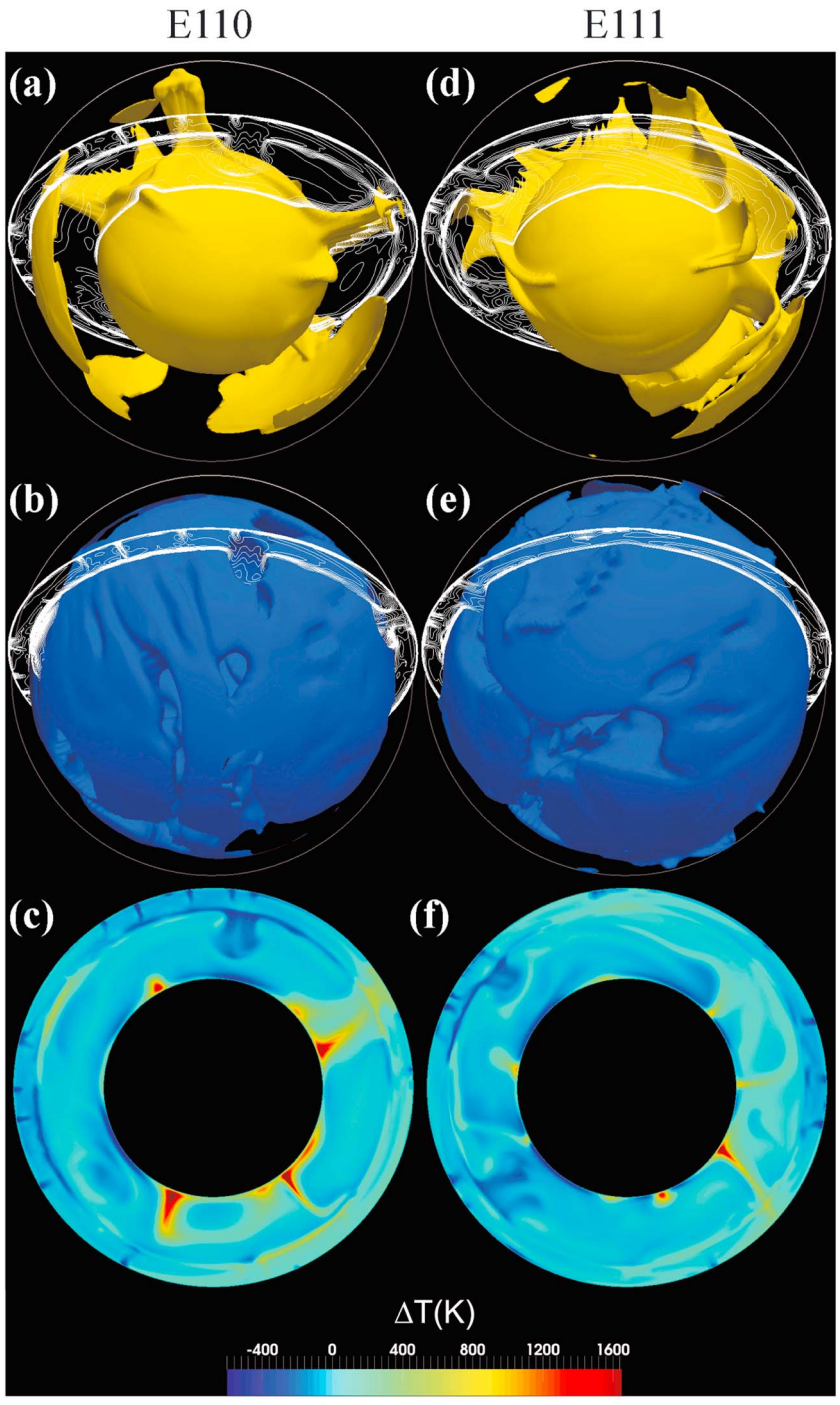

Figure 4. Temperature snapshots of the models E110 with two phase transitions at 410 km and 660 km depths and E111 with three phase transitions at 410 km, 660 km, and 2700 km depths. Superimposed slices of line contours provide a better visualization of the layered convection. The cold and hot isosurfaces (blue and yellow) have temperatures of 1575°K and 1875°K in the case of model E110 and 1725°K and 2025°K in the case of model E111. The bottom row display cross section of the temperature anomaly profiles.

analysis [e.g., *Butler and Peltier*, 2002] and the constraints required by double crossing of the pPv phase boundary in D″ layer [*Hernlund et al.*, 2005] restrict the heat flux from the core-mantle boundary; however, we have employed the same physical parameters and viscosity profiles to be able to compare our results with previously published axisymmetric spherical model results [*Shahnas and Peltier*, 2010].

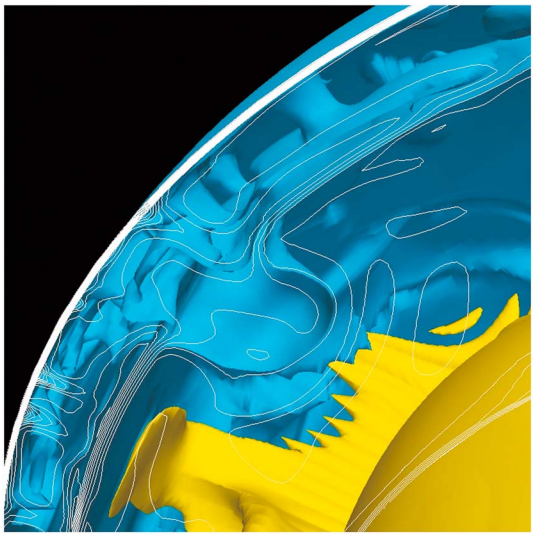

Figure 5. A close-up from a cut of model E111 displaying a mantle avalanche and a stagnated plume at 660 km endothermic phase transition depth. The cold isosurfaces (blue) have temperatures in the range of 1400°K–1725°K, and the hot isosurface (yellow) has a temperature of 2025°K.

A present-day internal heating rate of 13 TW (which is close to the requirement of chondritic meteorites; see *Butler and Peltier* [2002] for discussion) which is uniformly distributed throughout the mantle will be assumed for these models. At the external boundaries of the convecting mantle, the radial mass flux is assumed to vanish and free slip boundary conditions are imposed at both the CMB and surface. The surface and CMB are kept at constant temperatures 293°K and 4000°K, respectively. In the second and third models, we will assume slopes of 3.0 MPa/K and −3.0 MPa/K, together with density contrasts of 200 kg/m^3 and 440 kg/m^3 at the exothermic and endothermic phase transition boundaries at 410 km and 660 km depths, respectively. Our choices for the values of these phase transition parameters are based on our primary goal in this section which is to directly compare the results for radial layering obtained using the three-dimensional Yin-Yang grid-based model with those previously obtained in axisymmetric spherical geometry using exactly the same representations for all of the mineral physics parameters employed by *Shahnas and Peltier* [2010]. The phase transition parameters for the postperovskite deep-mantle phase transition in the third model are 12.0 MPa/K and 80 kg/m^3 for the slope and density contrast, respectively. The model results are summarized in Table 4 where they are compared with their axisymmetric spherical counterparts [*Shahnas and Peltier*, 2010]. This intercomparison is extremely important as it demonstrates a remarkable consistency between the CV-based 3-D model results and their axisymmetric spherical counterparts. The importance of this result resides in the fact that axisymmetric shell model results have previously been employed as the basis for analyses of planetary thermal history [e.g., *Butler and Peltier*, 2002].

Snapshots of temperature contours from the models E110 and E111 are shown in Figure 4. The hot upwelling plumes and cold downwellings are respectively shown by yellow and blue solid colors. The position of mantle "avalanches" in which cold material that has initially ponded in the mantle transition zone above the 660 km discontinuity spontaneously breaks through this horizon can be seen by inspection of the blue isosurfaces. In order to better display the downwelling patches and mantle avalanches that occur due to the modulation of the mixing process by the action of the endothermic phase transition at 660 km depth [*Peltier and Solheim*, 1992; *Solheim and Peltier*, 1993, 1994a, 1994b], we have suppressed the contours representing the downwellings at a radius of 5700 km which is the radius of the base of the "transition zone" which is defined by the presence of the endothermic spinel → perovskite + magnesiowüstite transition. Cross sections superimposed on both the cold and hot isosurfaces provide an improved visualization of the nature of the layered mantle convection process that is induced by the physical influence of this endothermic phase transition. The first column of Figure 4 displays hot and cold isosurfaces and a cross section of the E110 model with two phase transitions at 410 km and 660 km depths. The second column of this figure displays the model E111 with three phase transitions including the deep-mantle Pv-pPv exothermic phase transition. The cold and hot isosurfaces represent 1575°K and 1875°K temperatures in the case of the E110 model and 1725°K and 2025°K in the case of the E111 model. In both models, as can be verified on the basis of the white contours, the upwelling plumes become effectively stagnant at the 660 km horizon. However, there are regions in which these upwelling plumes do penetrate into the upper mantle. Similarly, although the downwelling cold mantle flow in the upper mantle stagnates at the level of the endothermic phase transition over a broad region, there are other regions in which the mantle flow does descend from the upper mantle into the lower mantle through the avalanche process. A close-up of a cut from E111 is displayed in Figure 5, which clearly demonstrates an avalanche event and plume stagnation at the 660 km phase transition boundary.

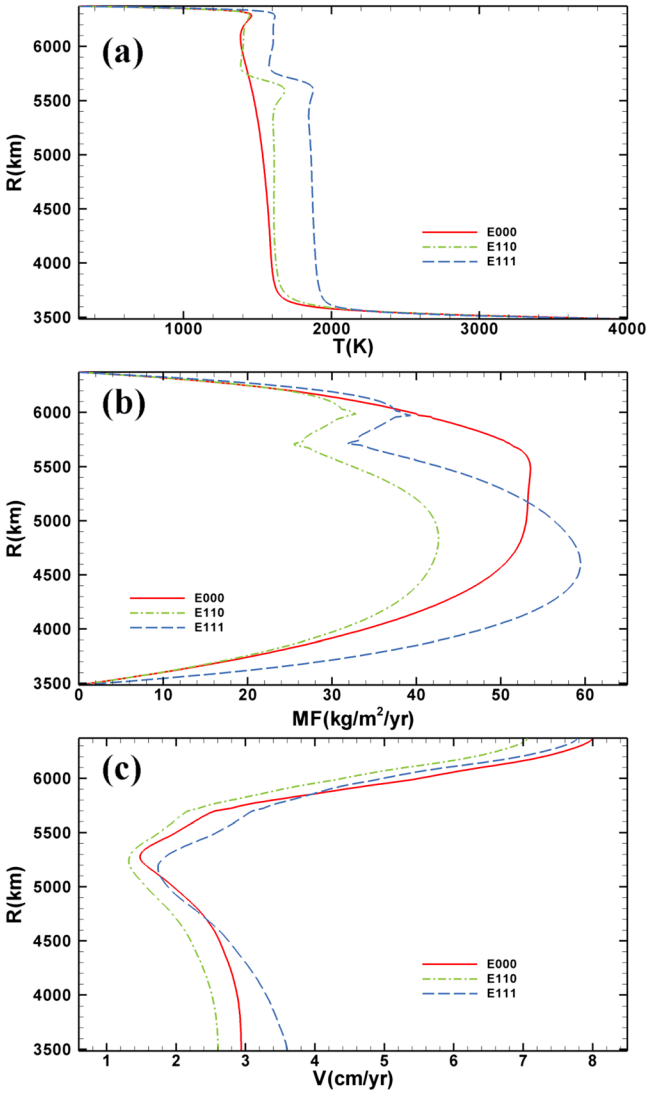

Figure 6. (a) A plot of mantle geotherms, (b) averaged radial mass fluxes, and (c) mean radial velocities for the Earth models E000 with no phase transition, E110 with two phase transitions at 410 km and 660 km depths and E111 with three phase transitions at 410 km, 660 km, and 2700 km depths.

Model E111 is obviously warmer than the E110 model due to the presence of the Pv-pPv deep-mantle phase transition which can also be verified on the basis of Figure 6a. The difference in mean temperature between these models is about 150°K. In both models E110 and E111, we observe very similar degrees of layering to that predicted by the previously analyzed axisymmetric models, as is evident on the basis of the time-averaged depth-dependent radial mass flux as in *Peltier and Solheim* [1992], namely

$$\frac{1}{T}\int_t F_m(r,t)\mathrm{d}t = \frac{1}{TS_r}\int_t \mathrm{d}t \int_{S_r} \rho |V_r| \mathrm{d}s, \tag{25}$$

where the time-dependent average mass flux is evaluated over the spherical surface S_r at radius r. From Figure 6b in both models with and without the Pv-pPv phase transition, we observe a mass flux reduction at the level of the 660 km endothermic phase transition. Compared to model E110, the number of instabilities at the surface of the CMB and therefore the number of rising plumes is larger in model E111 due to the presence of the deep-mantle Pv-pPv solid-solid phase transition and the vigor of mantle mixing and the mean mantle temperature is higher in the latter model. As can be verified from Figure 6b, although the upper mantle and the lower mantle in E110 and E111 are not sharply differentiated and there exists a finite degree of mixing between these two regions of the mantle, there is nevertheless an approximately 15 kg/m^2/yr reduction in mass flux at the endothermic transition level at 660 km depth (compared to E000). The new three-dimensional control volume results demonstrate that the episodically layered style of mantle mixing also persists in models which include the deep-mantle Pv-pPv phase transition as predicted for axisymmetric models [e.g., *Shahnas and Peltier*, 2010; *Shahnas et al.*, 2011]. Figure 6c compares the spherically averaged velocities for three models E000, E110, and E111. In the model with two phase transitions (E110), the average velocity at the CMB is lower than that in the E000 model; however, due to the presence of Pv-pPv phase transition in model E111, the average velocity at the CMB is higher in E111 than that in E000. The surface velocity for models E000, E110, and E111 are respectively 7.1, 5.4, and 6.6 cm/yr. Compared to the model with no phase transitions, while the presence of the endothermic phase transition at 660 km depth has reduced the surface velocity from 7.1 cm/yr to 5.4 cm/yr, the exothermic deep-mantle phase transition has to a large extent compensated for this impact. It is worth noting that for these models, which incorporate no impact due to the action of surface plates, the horizontal surface velocities are nevertheless in the range of those characteristic of present-day plate motions.

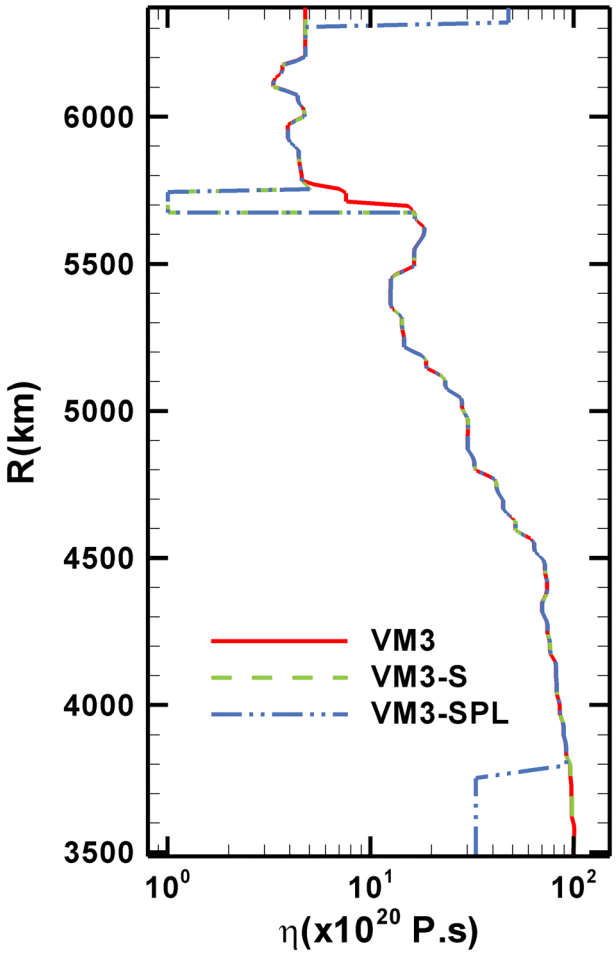

Figure 7. VM3 viscosity profile is compared with the modified versions of viscosity profiles VM3-S and VM3-SPL employed in E111-S (E111 with superplasticity at 660 km depth) and E111-SPLSCC (the same as E111-S but with lower CMB temperature of 3600°K and the endothermic Clapeyron slope of −2.8 MPa/K which includes also the HS-LS iron spin transition at mid mantle pressures), respectively.

In a second sequence of Earth models, we present two examples. The first model of this sequence, denoted E111-S, is basically the same as E111 except for the viscosity profile. The viscosity profile employed in E111-S is a modified version of VM3 in which a 70 km thick low-viscosity layer has been added to the radial profile in the endothermic phase transition zone as displayed in Figure 7, representing the presence of transformational superplasticity at the depth of this phase transition (VM3-S profile). The second model in this sequence, denoted by E111-SPLSCC, is similar to E111-S except that it also includes the HS-LS spin crossover in iron in the ferropericlase phase of mantle material. The spin-dependent data for ferropericlase used in this model are the same as were employed in our previous work [*Shahnas et al.*, 2011] and were provided by *Wu et al.* [2009]. In this model, a spin-dependent density anomaly of the following form was employed:

$$\Delta\rho_{\text{spin}} = \Delta\rho_s + \Delta\rho_\alpha + \Delta\rho_K, \tag{26}$$

where

$$\Delta\rho_\alpha = -\overline{\rho}\Delta\alpha_s(T - T_r) \tag{27}$$

and

$$\Delta\rho_K = \overline{\rho}\left[\left(\frac{1}{K_T + \Delta K_s} - \frac{1}{K_T}\right)(p - p_r)\right] \tag{28}$$

are added to the right-hand side of the state equation (5). $\Delta\rho_s$, $\Delta\alpha_s$, and ΔK_s are spin transition-induced pressure- and temperature-dependent anomalies as referenced by *Shahnas et al.* [2011]. The bulk modulus anomaly is the overall anomaly from ferropericlase and perovskite [*Catalli et al.*, 2010]. The CMB temperature and the endothermic Clapeyron slope for this model are assumed to be 3600°K [e.g., *Boehler*, 1992] and −2.8 MPa/K, respectively (note that although this was the slope initially determined experimentally for the spinel → perovskite + magnesiowüstite transition, we are employing the number here to represent the collective effect of all the phase transitions that occur near 660 km depth). The viscosity profile for this model VM3-SPL is a modified version of VM3. In the further viscosity profile VM3-SPL, we have simulated a 50 km lithosphere at the surface of the planet by increasing the viscosity by a factor of 10 in this upper layer. As in model E111-S, a low-viscosity layer is employed to simulate the influence of transformational superplasticity at the endothermic phase transition depth. Finally, the viscosity profile also includes a low-viscosity layer representing the viscosity reduction in the D″ layer at the bottom of mantle. The viscosity profiles for these models are displayed in Figure 7 on which they are compared with the original VM3 profile.

The geotherms, mass fluxes, and the spherically averaged velocities for these two models are compared with the similar quantities of E111 in Figure 8. Compared to E111, the inclusion of a superplastic layer at 660 km phase transition depth results in an approximately 40°–50°K decrease in midmantle temperature as well as an 8 kg/m^2/yr reduction in mass flux at 660 km depth in E111-S. This may be understood by virtue of the fact

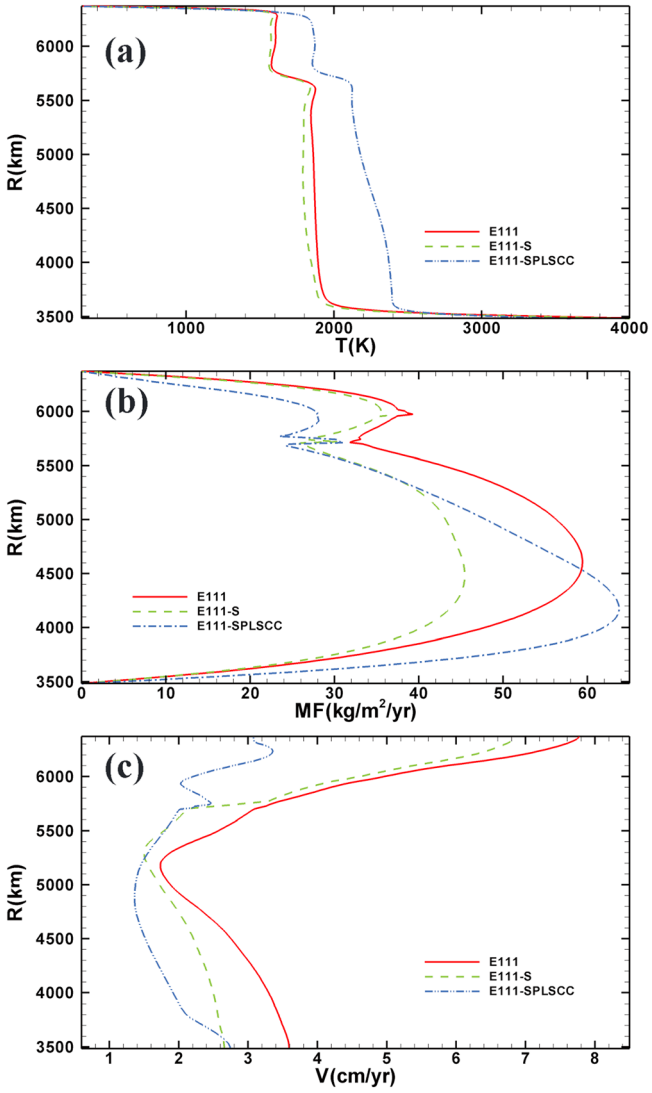

Figure 8. A plot of (a) mantle geotherms, (b) averaged radial mass fluxes, and (c) mean radial velocities for the Earth models E111, E111-S, and E111-SPLSCC.

that the strength of the endothermic phase transition barrier depends on the lateral variation in temperature and the fact that a low-viscosity layer at this depth enhances the lateral variations in temperature and therefore the topography of the phase boundary. However, a higher-viscosity reduction in this layer could finally increase the exchange of mass across 660 km depth due to the development of localized convective instabilities in this region.

It has been suggested that the iron spin transition in ferropericlase may have a significant impact on the style of mantle convection [*Shahnas et al.*, 2011; *Wu and Wentzcovitch*, 2014]. The spin transition in iron in the lower mantle minerals may increase the radial velocities and advective heat transport [*Bower et al.*, 2009]. The impacts of spin-driven iron partitioning on the dynamics of mantle convection have also been studied [*Vilella et al.*, 2014]. In this recent work, the authors have found that the RMS vertical velocities may increase by 15% and 6% for Al-free and Al-bearing systems, respectively. The transition occurs at midmantle pressures (60 to 70 GPa), and the hot rising plumes and cold downwelling slabs passing through this transition zone do experience a density change due to the iron spin crossover in mantle minerals [*Wu et al.*, 2009; *Shahnas et al.*, 2011]. This may result in a partial stagnation (weak stagnation) slowing the mantle flow passing through midmantle depths [*Shahnas et al.*, 2011]. Snapshots of temperature contours and cross sections from this model (E111-SPLSCC), which incorporates this recently experimentally discovered transition, are shown in Figure 9 in 25 Myr intervals (from left to right). Compared to E111, due to the presence of a lithospheric layer and a low-viscosity layer at the base of the mantle, in E111-SPLSCC, the mantle temperature is higher in this latter model (~330°K). However, additional warming occurs below the midlower mantle horizon (~1600 km depth) due to the combined impact of the additional iron spin transition in ferropericlase and viscosity reduction in the D″ layer (Figures 10 and 8a). This fact also can be seen in the cross sections from the E111-SPLSCC convection model (Figure 9, bottom row). The inclusion of a low-viscosity zone in the base of the mantle enhances the heat fluxes at the boundaries [e.g., *Shahnas and Peltier*, 2010]; however, the inclusion of a lithospheric layer of reduced mobility at the surface of the planet reduces the transport of heat to the upper surface and also across the CMB (in the statistically steady state).

Model results for the models E111-S and E111-SPLSCC are compared with the results of E111 in Table 5. In this final model, the mass exchange across the depth of the 660 km phase transition has been further decreased (Figure 8b). It has previously been shown that the iron spin crossover in mantle minerals could also cause weak flow stagnation at the midmantle level [*Shahnas et al.*, 2011] which is the direct

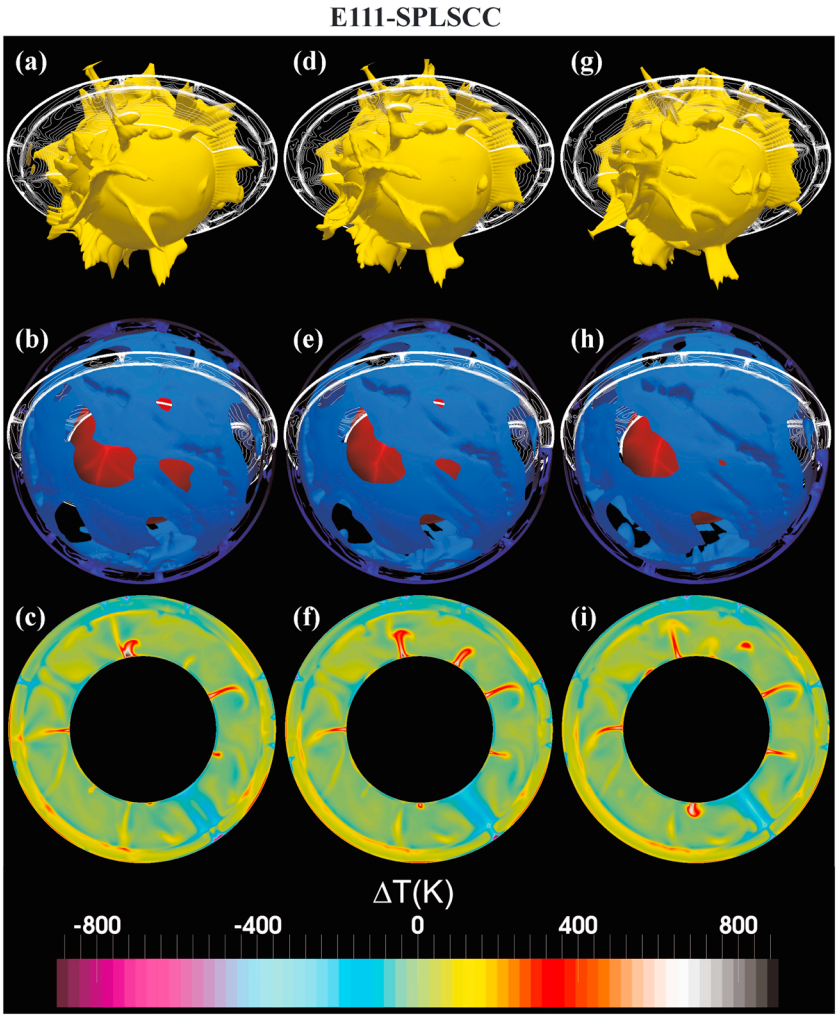

Figure 9. The snapshots of E111-SPLSCC model 25 Myr apart (from left to right). The cold and hot isosurfaces (blue and yellow) have temperatures of 2050°K and 2400°K. The bottom row display cross section of the temperature anomaly profiles.

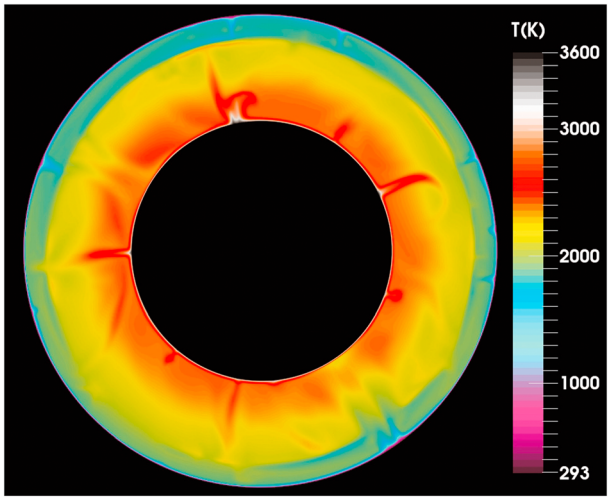

Figure 10. A cross section of E111-SPLSCC model shown in the first column of Figure 9, displaying the temperature gradient between the upper and lower regions in the lower mantle.

consequence of the buoyancy variation in the lower mantle region due to the action of the spin crossover in iron.

Figure 11 displays the time series of the temperature anomaly for a 2-D section of the E111-SPLSCC model in 25 Myr intervals. Inspection of Figures 11a–11f reveals that while the central plume rises upward and is deflected at 660 km depth by the impact of the endothermic phase transition at this level, the plume at the right of the image is deflected at the mid-mantle level (1600–1800 km depth range as indicated by grey circular lines) by the impact of the spin transition-induced density anomalies at spin crossover depths. The laminated plume (Figure 11e), after crossing the spin transition region, is then accelerated upward in shallower depths

Table 5. Time-Averaged Mantle Mean Temperature and Surface Heat Flux of the Models E111, E111-S, and E111-SPLSCC

Model	T (K)	HF_{surf} (TW)
E111	1748	63.7
E111-S	1728	60.7
E111-SPLSCC	2093	50.1

(Figure 11f) before losing its identity 50 Myr later (Figure 11g). Similarly, the mantle avalanche at the left of the image in Figure 11e that is passing through the 660 km depth phase transition boundary is deflected at the midmantle level (Figures 11f and 11g). The second avalanche through the 660 km depth phase transition boundary (that at the right of the image) is also deflected by the impact of the spin crossover at the midmantle horizon and remains for about 50 Myr between 1600 km and 1800 km depths. The cold patch is then accelerated downward, a phenomenon that has previously been referred to as a spin-induced midmantle avalanche (SIMMA) event [*Shahnas et al.*, 2011]. These midmantle avalanches are, however, rather uncommon and of modest strength. They are nevertheless detectable in the numerical models. Figure 12 displays the time series of another section from the most complex of our models. The frames of this figure also reveal that the downwelling cold material initiated by an avalanche event at the 660 km phase transition depth is stagnating at the midmantle level. The existence of such midmantle heterogeneities (interpreted as slab remnants with low sinking rate) has been identified in several geographical

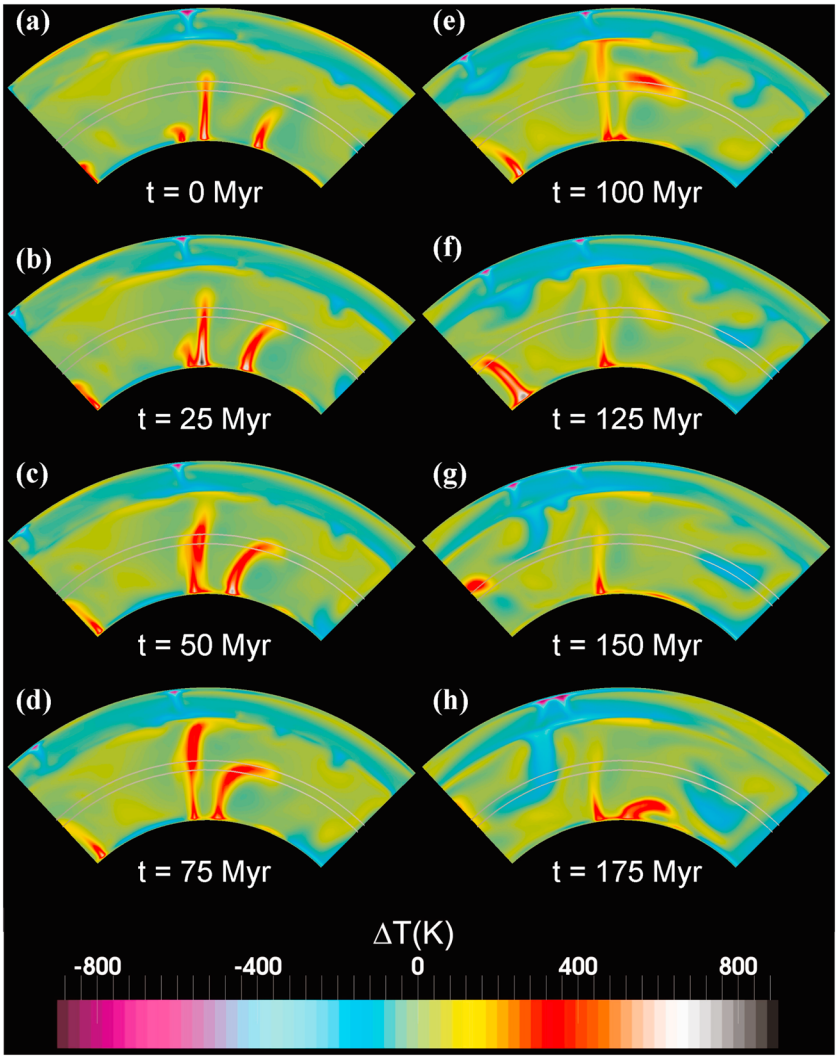

Figure 11. Time series of the temperature anomaly for a 2-D section of E111-SPLSCC model in 25 Myr intervals demonstrating plume and downwelling stagnation at midmantle horizon and a SIMMA event.

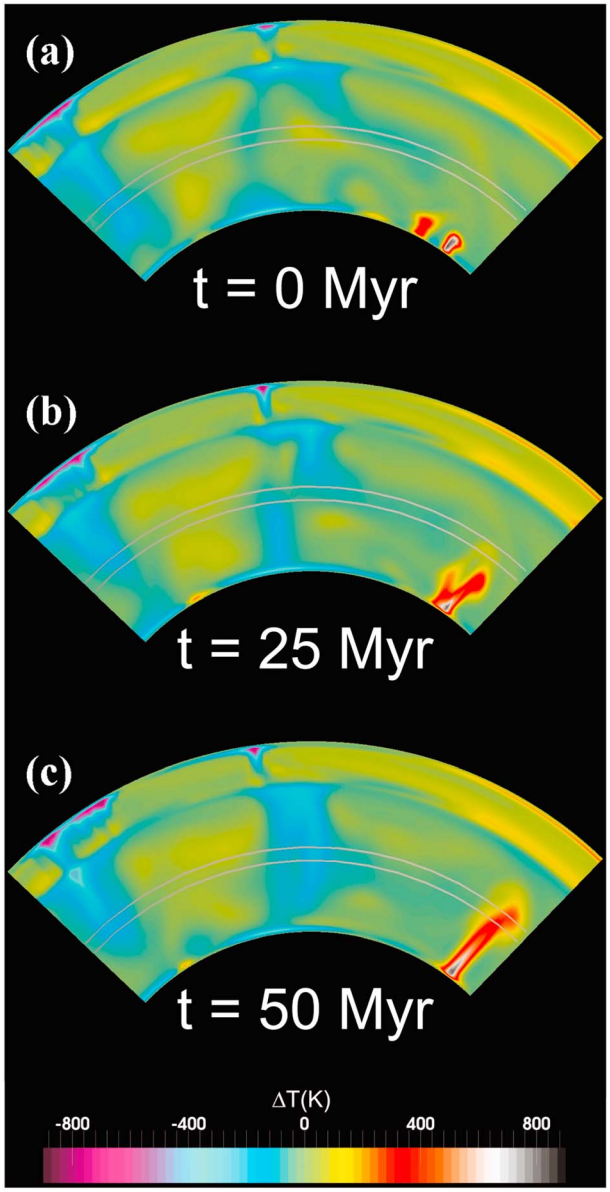

Figure 12. Time series of the temperature anomaly for a 2-D section of E111-SPLSCC model in 25 Myr intervals demonstrating a downwelling deflection and stagnation at spin crossover level with a lateral extent of more than 1500 km.

regions [e.g., *Van der Voo et al.*, 1999a, 1999b; *Li and Yuen*, 2014] which have previously been explained on the basis of rheological considerations as dynamically produced [e.g., *Jarvis and Lowman*, 2005; *Shahnas and Jarvis*, 2007; *Li and Yuen*, 2014]. We suggest that the existence of the spin crossover in the lower mantle may provide an alternative and more plausible interpretation of these enigmatic lower mantle structures.

7. Discussion

The efficiency of heat transfer plays a crucial role in the understanding of planetary thermal history and has been the subject of many previous analyses [e.g., *Sharp and Peltier*, 1979; *Solheim and Peltier*, 1993; *Sotin and Labrosse*, 1999; *Butler and Peltier*, 2002; *Shahnas et al.*, 2008]. The degree to which mantle convection model results are able to properly account for observed geological processes directly depends on the accuracy of the physical, chemical, and rheological parameters of the mantle material employed as model inputs. Our understanding of mantle material properties has drastically changed during the past decade due to the availability of the experimental results for mantle minerals under high-pressure and high-temperature conditions. The experimental discovery of Pv-pPv phase transition in the deep mantle is one example of the impact that high-pressure mineral physics discoveries are having on our understanding of deep-Earth structure. It has provided an alternative interpretation of the seismic heterogeneity in D″ that does not involve the compositional heterogeneity that was most often previously assumed [e.g., *Kellogg et al.*, 1999; *Li et al.*, 2014] or the existence of partial melt in the vicinity of the CMB [e.g., *Lay et al.*, 2004].

In the upper mantle and most of the upper part of the lower mantle, the variations of shear and bulk sound velocities (V_s and V_ϕ, respectively) are well correlated; however, in the deepest lower mantle, they are poorly correlated and most often are in fact anticorrelated [*Su and Dziewonski*, 1997; *Masters et al.*, 2000], an observation that is not comprehensible in terms of the temperature dependence of these elastic properties alone. To a significant degree, the observed anticorrelation between V_s and V_ϕ in the D″ region can be explained by the Pv-pPv transition [*Trampert et al.*, 2004; *Wentzcovitch et al.*, 2006]. Further discussion of the significance of the Pv-pPv transition to the understanding of the inferred properties of D″ will be found in *Shahnas and Peltier* [2010].

The significance of the discovery of the iron spin transition in ferropericlase, the second most abundant mineral of the lower mantle, at midmantle pressures, is associated with the fact that it may provide a similarly

important noncompositional explanation for the observed decorrelation of V_p and V_s that develops at midlower mantle depths. Extensive work on the HS-LS spin crossover in iron in ferropericlase has revealed that most of the properties of mantle material are affected by this deep-mantle phenomenon [e.g., *Lin and Tsuchiya*, 2008; *Wentzcovitch et al*., 2009; *Marquardt et al*., 2009; *Antonangeli et al*., 2011; *Wu et al*., 2013; *Wu and Wentzcovitch*, 2014]. Weak anticorrelation between the shear velocity (V_s) and bulk sound velocity (V_ϕ) has been observed at the shallower depths of the lower mantle [*Masters et al*., 2000; *Ishii and Tromp*, 2001]. Such anticorrelation between V_s and V_ϕ has recently been predicted as a consequence of the spin crossover in ferropericlase which occurs at midlower mantle depths [*Wu and Wentzcovitch*, 2014]. This decorrelation is now commonly interpreted as requiring compositional stratification and has led to a continuing plethora of models based upon the assumption that mantle mixing must be a consequence of thermochemical convection. The work of *Wu and Wentzcovitch*, 2014 suggests that models of this kind may not be required to explain the inferred decorrelation. Although chemical heterogeneity at some level must clearly exist in the mantle [e.g., see *Stixrude and Lithgow-Bertelloni*, 2012, for a review], it is a highly significant issue as to the extent to which such heterogeneity exerts significant control on the mantle general circulation. In this paper, we have attempted to further describe the manner in which the spin transition may contribute in an important way to the details of the mixing phenomenon.

We have also presented new CV-based results on the degree of layering of the convective circulation to be expected in the solid mantle of the Earth. The results are based on the new 3-D control volume-based spherical convection code with overlapping Yin-Yang grids which includes the influence of compressibility in the anelastic approximation, solid-solid phase transitions, transformational superplasticity, the iron spin transition, large variations of material properties, and nonlinear rheology. The test models described in section 4 were employed to demonstrate the consistency between the results of this CV-based code with previously published results for benchmark problems and the capability of this new CV-based software to accurately account for the impacts of large variations in viscosity in both the radial and azimuthal directions. We have obtained extremely good agreement between the new control volume-based results and previously published benchmark results [*Zhong et al*., 2008; *Yoshida and Kageyama*, 2004; *Ratcliff et al*., 1996a; *Iwase*, 1996; *Tabata and Suzuki*, 2000; *Kameyama et al*., 2008; *Tackley*, 2008; *Stemmer et al*., 2006]. In further work, we intend to explore the additional impacts due to the strong lateral variations of viscosity that are expected to accompany the convective mixing process. The results presented in this paper will be employed to provide a point of comparison with models from which this additional source of complexity has been eliminated.

The first sequence of the Earth models discussed in section 6 based upon the use of the VM3 radial viscosity profile and complex variations of thermodynamic properties [*Fei*, 1995; *Hofmeister*, 1999; *Schmeling et al*., 2003], which also include the influence of upper mantle exothermic and endothermic phase transitions as well as the recently recognized deep-mantle exothermic phase transition [*Murakami et al*., 2004], were analyzed using fully three-dimensional configurations. Our analyses based upon the application of the CV formulation of the convection process demonstrated that the mean field characteristics of otherwise identical models were extremely close to one another, the axisymmetric results being those from a previously published analysis [*Shahnas and Peltier*, 2010]. Similar to their axisymmetric counterparts, the CV-based spherical models demonstrate that, although the presence of the newly discovered deep-mantle Pv-pPv phase transition enhances the vigor of circulation and the nature of the interaction between the upper and lower mantles and to some extent impacts the degree of radial layering, the layered pattern of convection does persist even in the models having higher Clapeyron slope for the Pv-pPv transition than that which appears to be constrained experimentally. As demonstrated in our previously published axisymmetric models [e.g., *Shahnas and Peltier*, 2010], our control volume spherical model results demonstrate that this new solid-solid phase transition could significantly impact mantle dynamics and thus the cooling of the core and the thermal history of the planet. In the model E111-S with transformational superplasticity (grain size related softening) at the endothermic phase transition at 660 km depth, there is an enhancement in layering. Similar enhancement in layering is observed in the final model E111-SPLSCC which further incorporates the impact of the iron spin transition in ferropericlase.

Based on the results of our final model (E111-SPLSCC), the subducted cold mantle material that eventually descends through the endothermic horizon at 660 km depth is expected to stagnate at the midmantle level (~1700 km). The spin crossover in the lower mantle may offer an alternative dynamical explanation for a number of enigmatic lower mantle features and structures such as the thermal anomalies that have been imaged tomographically below India and Tibet [*Van der Voo et al*., 1999b] in the framework of an

isochemical convection model. The northernmost anomaly under India/Tibet at a relatively shallow depth is approximately 141 Myr old [*Besse and Courtillot*, 1988] and is believed to be the remnant of a mature subduction zone, having ingested some 4000 km of the Paleo-Tethys seafloor. The high *P* wave velocity anomalies in the deep mantle under Siberia, around the Pacific, and under the Mediterranean-Himalaya-Indonesian belt are also interpreted as the remnants of subducted slabs [*Van der Voo et al*., 1999a]. The heterogeneities detected in the depth range of 930–1120 km under northern China and the Japan Sea located to the east of the hinge of the stagnant Pacific slab may also be related to the remnants of the ancient subducted basaltic crust and the Izanagi plate [*Li and Yuen*, 2014]. A similar anomaly is located to the west of Lake Baikal, a remnant of the Mongol-Okhost subduction zone. Efforts have been made to explain these enigmatic midmantle thermal anomalies by invoking the effects of viscosity stratification or local viscosity constraints as a possibility [e.g., *Jarvis and Lowman*, 2005; *Shahnas and Jarvis*, 2007; *Li and Yuen*, 2014]. However, the sinking rates of slabs truncated by continental collision in some of these regions, in particular under India/Tibet, based on their present configuration cannot be explained by a modest viscosity increase across the mantle and would require a viscosity increase by three orders of magnitude [*Shahnas and Jarvis*, 2007]. An increase of viscosity in this range of midmantle depths inferred on the basis of the analysis of glacial isostatic adjustment observations [*Peltier and Drummond*, 2010] is modest and cannot account for these interpreted sinking rates. The spin transition-induced stagnation of mantle flow above the midmantle horizon may offer an alternative explanation of the time delay required to explain this observation in terms of a fossil slab without the necessity of appealing to an extremely sharp increase of viscosity at midmantle depth.

Probably the most important of the new results reported in this paper, however, are those describing the impact in a high-resolution three-dimensional model of the iron spin transition. As discussed in detail in the recent paper by *Wu and Wentzcovitch* [2014], there is good reason to believe that the seismological evidence previously invoked to suggest the presence in the lower half of the lower mantle of chemical heterogeneity may in fact be due to the isochemical spin transition in iron. In our view, this is an extremely important result of the high-pressure ab initio calculation of the impact of the spin transition on mantle elastic properties that these authors have performed. Although the existence of chemical heterogeneity within the mantle would appear to be inevitable at some level, it may not be sufficient to be exerting first-order control on the circulation. Our analysis of the impact of the spin transition on isochemical mixing has furthermore demonstrated that when this transition is combined with the upper mantle phase transitions, the layering of the circulation is further enhanced, implying that even with the reduced value of the Clapeyron slope of the endothermic transition preferred on the basis of the most recent high-pressure experiments, highly significant layering of the flow at 660 km depth is to be expected, as is implied by high-resolution subduction zone tomographic analyses.

Appendix A

In spherical polar coordinates, the three components of the momentum equation are simply given by

$$F_r = -\frac{\partial P}{\partial r} + \frac{1}{r^2}\frac{\partial}{\partial r}\left(r^2\tau_{rr}\right) + \frac{1}{r\sin(\theta)}\frac{\partial}{\partial\theta}\left(\sin(\theta)\tau_{r\theta}\right) + \frac{1}{r\sin(\theta)}\frac{\partial}{\partial\varphi}\tau_{r\varphi} - \frac{\tau_{\theta\theta}+\tau_{\varphi\varphi}}{r} - R_o\rho g = 0, \tag{A1}$$

$$F_\theta = -\frac{1}{r}\frac{\partial P}{\partial\theta} + \frac{1}{r^2}\frac{\partial}{\partial r}\left(r^2\tau_{r\theta}\right) + \frac{1}{r\sin(\theta)}\frac{\partial}{\partial\theta}\left(\sin(\theta)\tau_{\theta\theta}\right) + \frac{1}{r\sin(\theta)}\frac{\partial}{\partial\varphi}\tau_{\theta\varphi} + \frac{\tau_{r\theta}}{r} - \frac{\cot(\theta)}{r}\tau_{\varphi\varphi} = 0, \tag{A2}$$

$$F_\varphi = -\frac{1}{r\sin(\theta)}\frac{\partial P}{\partial\varphi} + \frac{1}{r^2}\frac{\partial}{\partial r}\left(r^2\tau_{r\varphi}\right) + \frac{1}{r\sin(\theta)}\frac{\partial}{\partial\theta}\left(\sin(\theta)\tau_{\varphi\theta}\right) + \frac{1}{r\sin(\theta)}\frac{\partial}{\partial\varphi}\tau_{\varphi\varphi} + \frac{\tau_{r\varphi}}{r} + \frac{\cot(\theta)}{r}\tau_{\theta\varphi} = 0, \tag{A3}$$

in which the components of the stress tensor are

$$\tau_{rr} = 2\eta \frac{\partial V_r}{\partial r} - \frac{2}{3}\eta\left(\nabla \cdot \vec{V}\right), \tag{A4}$$

$$\tau_{\theta\theta} = 2\eta\left(\frac{V_r}{r} + \frac{1}{r}\frac{\partial V_\theta}{\partial \theta}\right) - \frac{2}{3}\eta\left(\nabla \cdot \vec{V}\right), \tag{A5}$$

$$\tau_{\varphi\varphi} = 2\eta\left(\frac{V_r}{r} + \frac{V_\theta}{r}\cot(\theta) + \frac{1}{r\sin(\theta)}\frac{\partial V_\varphi}{\partial \varphi}\right) - \frac{2}{3}\eta\left(\nabla \cdot \vec{V}\right), \tag{A6}$$

$$\tau_{r\theta} = \tau_{\theta r} = \eta\left(\frac{\partial V_\theta}{\partial r} + \frac{1}{r}\frac{\partial V_r}{\partial \theta} - \frac{V_\theta}{r}\right), \tag{A7}$$

$$\tau_{\theta\varphi} = \tau_{\varphi\theta} = \eta\left(\frac{\sin(\theta)}{r}\frac{\partial}{\partial \theta}\left(\frac{V_\varphi}{\sin(\theta)}\right) + \frac{1}{r\sin(\theta)}\frac{\partial V_\theta}{\partial \varphi}\right), \tag{A8}$$

$$\tau_{\varphi r} = \tau_{r\varphi} = \eta\left(\frac{1}{r\sin(\theta)}\frac{\partial V_r}{\partial \varphi} + r\frac{\partial}{\partial r}\left(\frac{V_\varphi}{r}\right)\right). \tag{A9}$$

Acknowledgments

The computations on which the paper is based were performed on the SciNet facility for High Performance Computation at the University of Toronto which is a component of the Compute Canada HPC platform. Additional support was provided by NSERC Discovery grant A9627 to W.R.P. The data used in this paper are available from the authors upon request.

References

Antonangeli, D., J. Siebert, C. Aracne, D. Farber, A. Bosak, M. Hoesch, M. Krisch, F. Ryerson, G. Fiquet, and J. Badro (2011), Spin crossover in ferropericlase at high pressure: A seismologically transparent transition?, *Science*, *331*(6013), 64–67.

Bachvar, A. A., and Z. A. Sviderskaya (1945), Izv. Akad. Nauk SSSR Otd. Tekh. Nauk, 9, 821.

Badro, J. (2012), A new spin on Earth's deep mantle, *Eur. Phys. Soc., EDP Sci.*, *43*, 18–21, doi:10.1051/epn/2012102.

Badro, J., G. Fiquet, F. Guyot, J.-P. Rueff, V. V. Struzhkin, G. Vanko, and G. Monaco (2003), Iron partitioning in Earth's mantle: Toward a deep lower mantle discontinuity, *Science*, *300*, 89–791.

Badro, J., G. Fiquet, and F. Guyot (2005), Thermochemical state of the lower mantle: New insights from mineral physics, in *Earth's Deep Mantle: Structure, Composition, and Evolution*, *Geophys. Monogr. Ser.*, vol. 160, edited by R. D. van der Hilst et al., pp. 241–260, AGU, Washington, D. C.

Balachandar, S., and D. A. Yuen (1994), Three-dimensional fully spectral numerical method for mantle convection with depth-dependent properties, *J. Comput. Phys.*, *132*, 62–74.

Balachandar, S., D. A. Yuen, and D. M. Reuteler (1996), High Rayleigh number convection at infinite Prandtl number with weakly temperature-dependent viscosity, *Geophys. Astrophys. Fluid Dyn.*, *83*(1–2), 79–117.

Baumgardner, J. R. (1985), 3-Dimensional treatment of convective flow in the Earth's mantle, *J. Stat. Phys.*, *39*(5–6), 501–511.

Besse, J., and V. Courtillot (1988), Paleogeographic maps of the continents bordering the Indian Ocean since the Early Jurassic, *J. Geophys. Res.*, *93*, 11,791–11,808, doi:10.1029/JB093iB10p11791.4.

Boehler, R. (1992), Melting of the Fe-FeO and the Fe-FeS systems at high pressure: Constraints on core temperatures, *Earth Planet. Sci. Lett.*, *111*, 217–227.

Bower, D. J., M. Gurnis, J. M. Jackson, and W. Sturhahn (2009), Enhanced convection and fast plumes in the lower mantle induced by the spin transition in ferropericlase, *Geophys. Res. Lett.*, *36*, L10306, doi:10.1029/2009GL037706.

Brunet, D., and P. Machetel (1998), Large-scale tectonics features induced by mantle avalanches with phase, temperature, and pressure lateral variations of viscosity, *J. Geophys. Res.*, *103*, 4929–4945, doi:10.1029/97JB01357.

Bunge, H.-P., M. A. Richards, and J. R. Baumgardner (1997), A sensitivity study of three dimensional spherical mantle convection at 108 Rayleigh number: Effects of depth-dependent viscosity, heating mode and an endothermic phase change, *J. Geophys. Res.*, *102*, 11,991–12,007, doi:10.1029/96JB03806.

Burns, R. G. (1993), *Mineralogical Application of Crystal Field Theory*, Cambridge Univ. Press, Cambridge, U. K., doi:10.1017/CBO9780511524899.

Butler, S. L., and W. R. Peltier (2002), Thermal evolution of Earth: Models with time-dependent layering of mantle convection which satisfy the Urey ratio constraint, *J. Geophys. Res.*, *107*(B6), 2109, doi:10.1029/2000JB000018.

Cammarano, F., H. Marquardt, S. Speziale, and P. J. Tackley (2010), Role of iron spin transition in ferropericlase on seismic interpretation: A broad thermochemical transition in the mid mantle?, *Geophys. Res. Lett.*, *37*, L03308, doi:10.1029/2009GL041583.

Catalli, K., S.-H. Shim, V. B. Prakapenka, J. Zhao, W. Sturhahn, P. Chow, Y. Xiao, H. Liu, H. Cynn, and W. J. Evans (2010), Spin transition in ferric iron in $MgSiO_3$ perovskite and its effect on elastic properties, *Earth Planet. Sci. Lett.*, *289*, 68–75.

Christensen, U. (1982), Phase boundaries in finite amplitude mantle convection, *Geophys. J. R. Astron. Soc.*, *68*, 487–491.

Christensen, U., and H. Harder (1991), 3-D convection with variable viscosity, *Geophys. J. Int.*, *104*(1), 213–226.

Christensen, U., and D. A. Yuen (1989), Time-dependent convection with non-Newtonian viscosity, *J. Geophys. Res.*, *94*(B1), 814–820, doi:10.1029/JB094iB01p00814.

Christensen, U. R. (1984), Convection with pressure- and temperature-dependent non-Newtonian rheology, *Geophys. J. R. Astron. Soc.*, *77*, 343–384.

Christensen, U. R. (1995), Effect of phase transitions on mantle convection, *Annu. Rev. Earth Planet. Sci.*, *23*, 65–87.

Christensen, U. R., and D. A. Yuen (1984), The interaction of a subducting lithospheric slab with a chemical or phase boundary, *J. Geophys. Res.*, *89*(B6), 4389–4402, doi:10.1029/JB089iB06p04389.

Christensen, U. R., and D. A. Yuen (1985), Layered convection induced by phase transitions, *J. Geophys. Res.*, *90*(B12), 10,291–10,300, doi:10.1029/JB090iB12p10291.

Cohen, R. E., I. I. Mazin, and D. Isaak (1997), Magnetic collapse in transition metal oxides at high pressure: Implications for the Earth, *Science*, *275*, 654–657, doi:10.1126/science.275.5300.654.
Collins, W. D., et al. (2006), The Community Climate System Model: CCSM3, *J. Clim.*, *19*, 2122–2143.
Fei, Y. (1995), in *Thermal Expansion, in Mineral Physics & Crystallography—A Handbook of Physical Constants*, *AGU Ref. Shelf*, vol. 2, edited by T. J. Ahrens, pp. 64–97, AGU, Washington, D. C.
Forte, A. M., and W. R. Peltier (1994), The kinematics and dynamics of poloidal-toroidal coupling in mantle flow: The importance of surface plates and lateral viscosity variations, *Adv. Geophys.*, *36*, 1–119.
Forte, A. M., A. M. Dziewonski, and R. L. Woodward (1993), A spherical structure of the mantle, tectonic plate motions, nonhydrostatic geoid, and topography of the core mantle boundary, in *Dynamics of Earth's Deep Interior and Earth Rotation*, *Geophys. Monogr. 72 IUGG*, vol. 12, edited by J.-L. Movel, D. E. Smylie, and T. Herring, pp. 135–166, AGU, Washington, D. C.
Fyfe, W. S. (1960), The possibility of delectron coupling in olivine at high pressures, *Geochim. Cosmochim. Acta*, *19*, 141–143, doi:10.1016/0016-7037(60)90046-6.
Glatzmaier, G. A. (1988), Numerical simulations of mantle convection: Time-dependent, three-dimensional, compressible, spherical shell, *Geophys. Astrophys. Fluid Dyn.*, *43*(2), 223–264.
Harder, H., and U. Hansen (2005), A finite-volume solution method for thermal convection and dynamo problems in spherical shells, *Geophys. J. Int.*, *161*, 522–537.
Harlow, F. H., and E. Welch (1965), Numerical calculation of time-dependent viscous flow of fluid with free surface, *Phys. Fluids*, *8*(12), 2182–2189.
Hernlund, J. W., C. Thomas, and P. J. Tackley (2005), A doubling of the post-perovskite phase boundary and structure of the Earth's lowermost mantle, *Lett. Nat.*, *434*, 882–886.
Hofmeister, A. M. (1999), Mantle values of thermal conductivity and the geotherm from phonon lifetimes, *Science*, *283*, 1699–1706.
Honda, S., D. A. Yuen, S. Balachandar, and D. Reuteler (1993), Three-dimensional instabilities of mantle convection with multiple phase transitions, *Sciences*, *259*, 1308–1311.
Ishii, M., and J. Tromp (1999), Normal-mode and free-air gravity constraints on lateral variations in velocity and density of Earth's mantle, *Science*, *285*, 20.
Ishii, M., and J. Tromp (2001), Even-degree lateral variations in the Earth's mantle constrained by free oscillations and the free-air gravity anomaly, *Geophys. J. Int.*, *145*(1), 77–96.
Iwase, Y. (1996), Three-dimensional infinite Prandtl number convection in a spherical shell with temperature-dependent viscosity, *J. Geomagn. Geoelectr.*, *48*, 1499–1514.
Jarvis, G. T., and J. P. Lowman (2005), Sinking slabs below fossil subduction zones, *Phys. Earth Planet. Inter.*, *152*, 103–115.
Jarvis, G. T., and D. P. McKenzie (1980), Convection in a compressible fluid with infinite Prandtl number, *J. Fluid Mech.*, *96*, 515–583.
Jarvis, G. T., and W. R. Peltier (1982), Mantle convection as a boundary layer phenomenon, *Geophys. J. R. Astron. Soc.*, *68*, 389–427.
Kageyama, A., and T. Sato (2004), The "yin-yang grid": An overset grid in spherical geometry, *Geochem. Geophys. Geosyst.*, *5*, Q09005, doi:10.1029/2004GC000734.
Kameyama, M., A. Kageyama, and T. Sato (2008), Multigrid-based simulation code for mantle convection in spherical shell using Yin Yang grid, *Phys. Earth Planet. Inter.*, *171*, 19–32.
Kellogg, L. H., B. H. Hager, and R. D. van der Hilst (1999), Compositional stratification in the deep mantle, *Science*, *283*, 1881–1884, doi:10.1126/science.283.5409.1881.
King, S. D., A. Raefsky, and B. H. Hager (1990), ConMan: Vectorizing a finite element code for incompressible two-dimensional convection in the Earth's mantle, *Phys. Earth Planet. Inter.*, *59*, 195–20.
Kumar, M. (2000), Equation of state and bulk modulus under the effect of high pressure-high temperature, *Phys. Chem. Miner.*, *27*, 650–655.
Lay, T., E. J. Garnero, and Q. Williams (2004), Partial melting in a thermochemical boundary layer at the base of the mantle, *Phys. Earth Planet. Inter.*, *146*, 441–467.
Li, J., and D. A. Yuen (2014), Mid-mantle heterogeneities associated with Izanagi plate: Implications for regional mantle viscosity, *Earth Planet. Sci. Lett.*, *385*, 137–144.
Li, X., D. Chen, X. Peng, F. Xiao, and X. Chen (2006), Implementation of the semi-Lagrangian advection scheme on a quasi-uniform overset grid on a sphere, *Adv. Atmos. Sci.*, *23*(5), 792–801.
Li, Y., F. Deschamps, and P. J. Tackley (2014), The stability and structure of primordial reservoirs in the lower mantle: Insights from models of thermochemical convection in three-dimensional spherical geometry, *Geophys. J. Int.*, *199*, 914–930.
Lin, J. F., and T. Tsuchiya (2008), Spin transition of iron in the Earth's lower mantle, *Phys. Earth Planet. Inter.*, *170*, 248–259, doi:10.1016/j.pepi.2008.01.005.
Lin, J. F., et al. (2008), Intermediate-spin ferrous iron in lowermost mantle post-perovskite and perovskite, *Nat. Geosci.*, *1*, 688–691, doi:10.1038/ngeo310.
Machetel, P., and P. Weber (1991), Intermittent layered convection in a model with an endothermic phase change at 670 km, *Nature*, *350*, 55–57.
Machetel, P., M. Rabinowicz, and P. Bernadet (1986), Three dimensional convection in spherical shells, *Geophys. Astrophys. Fluid Dyn.*, *37*, 57–84.
Machetel, P., C. Thoraval, and D. Brunet (1995), Spectral and geophysical consequences of 3-D spherical mantle convection with an endothermic phase-change at the 670 km discontinuity, *Phys. Earth Planet. Inter.*, *88*(1), 43–51.
Maehara, Y., and T. G. Langdon (1990), Review superplasticity in ceramics, *J. Mater. Sci.*, *25*, 2275–2286.
Marquardt, H., S. Speziale, H. J. Reichmann, D. J. Frost, F. R. Schilling, and E. J. Garnero (2009), Elastic shear anisotropy of ferropericlase in Earth's lower mantle, *Science*, *324*(5924), 224–226.
Masters, G., G. Laske, H. Bolton, and A. M. Dziewonski (2000), The relative behavior of shear velocity, bulk sound speed, and compressional velocity in the mantle: Implications for chemical and thermal structure, in *Earth's Deep Interior: Mineral Physics and Tomography From the Atomic to the Global Scale*, *Geophys Monogr. Ser.*, vol. 117, edited by S.-I. Karato et al., pp. 63–87, AGU, Washington, D. C.
McKenzie, D. P., J. M. Roberts, and N. O. Weiss (1974), Convection in the Earth's mantle: Towards a numerical solution, *J. Fluid Mech.*, *62*, 465–538.
Meike, A. (1993), A critical review of investigations into transformation plasticity, in *Defects and Processes in the Solid State: Geoscience Applications*, edited by J. N. Bolard and J. D. Fitz Gerald, pp. 5–25, Elsevier Science, Amsterdam.
Monnereau, M., and S. Quere (2001), Spherical shell models of mantle convection with tectonic plates, *Earth Planet. Sci. Lett.*, *184*, 575–587.
Moresi, L., and M. Gurnis (1996), Constraints on the lateral strength of slabs from three-dimensional dynamic flow models, *Earth Planet. Sci. Lett.*, *138*, 15–28.

Murakami, M., K. Hirose, K. Kawamura, N. Sata, and Y. Ohishi (2004), Post-perovskite phase transition in $MgSiO_3$, *Science*, *304*, 855–858.
Ogawa, M., G. Schubert, and A. Zebib (1991), Numerical simulations of 3-dimensional thermal convection in a fluid with strongly temperature-dependent viscosity, *J. Fluid Mech.*, *233*, 299–328.
Orszag, S. A. (1969), Numerical methods for the simulation of turbulence, *Phys. Fluids Supp. II*, *12*, 250–257.
Pari, G., and W. R. Peltier (1995), The heat flow constraint on mantle tomography based convection models: Towards a geodynamically self-consistent inference of mantle viscosity, *J. Geophys. Res.*, *100*(B7), 12,731–12,751, doi:10.1029/95JB01078.
Pari, G., and W. R. Peltier (1996), The free air gravity constraint on sub-continental mantle dynamics, *J. Geophys. Res.*, *101*(B12), 28,105–28,132, doi:10.1029/96JB02099.
Pari, G., and W. R. Peltier (1998), Global surface heat flux anomalies from seismic tomography-based models of mantle flow: Implications for mantle convection, *J. Geophys. Res.*, *103*(B10), 23,743–23,780, doi:10.1029/98JB01668.
Parmentier, E. M., D. L. Turcotte, and K. E. Torrance (1975), Numerical experiments on the structure of mantle plumes, *J. Geophys. Res.*, *80*(32), 4417–4425, doi:10.1029/JB080i032p04417.
Patankar, S. V. (1980), *Numerical Heat Transfer and Fluid Flow*, Hemisphere Publishing Corporation, Bristol, Pa.
Patankar, S. V., and D. B. Spalding (1972), A calculation procedure for heat, ass and momentum transfer in three-dimensional parabolic flows, *Int. J. Heat Mass Transfer*, *15*, 1787–1806.
Pearson, C. E. (1934), The viscous properties of lead-tin and bismuth-tin, *J. Inst. Met.*, *54*, 111.
Peltier, W. R. (1972), Penetrative convection in the planetary mantle, *Geophys. Astrophys. Fluid Dyn.*, *5*, 338–346.
Peltier, W. R. (1986), Deglaciation induced vertical motion of the North American continent and transient lower mantle rheology, *J. Geophys. Res.*, *91*(B9), 9099–9123, doi:10.1029/JB091iB09p09099.
Peltier, W. R. (1988), Lithospheric thickness, Antarctic deglaciation history and ocean basin discretization effects in a global model of postglacial sea level change, *Quat. Res.*, *29*, 93–112.
Peltier, W. R. (1998a), The inverse problem for mantle viscosity, *Inverse Probl.*, *14*, 441–478.
Peltier, W. R. (1998b), Postglacial variations in the level of the sea: Implications for climate dynamics and solid earth geophysics and climate system dynamics, *Rev. Geophys.*, *36*, 603–689, doi:10.1029/98RG02638.
Peltier, W. R., and R. Drummond (2010), Deepest mantle viscosity: Constraints from Earth rotation anomalies, *Geophys. Res. Lett.*, *37*, L12304, doi:10.1029/2010GL043219.
Peltier, W. R., and L. P. Solheim (1992), Mantle phase transitions and layered chaotic convection, *Geophys. Res. Lett.*, *19*(3), 321–324, doi:10.1029/91GL02951.
Peltier, W. R., S. Butler, and L. P. Solheim (1997), The influence of phase transformations on mantle mixing and plate tectonics, in *Earths Deep Interior*, edited by D. J. Crossley, Taylor and Francis, U. K.
Poirier, J.-P. (1985), *Creep of Crystals*, 264 pp., Cambridge Univ. Press, Cambridge.
Ratcliff, J. T., G. Schubert, and A. Zebib (1996a), Steady tetrahedral and cubic patterns of spherical-shell convection with temperature-dependent viscosity, *J. Geophys. Res.*, *101*, 25,473–25,484, doi:10.1029/96JB02097.
Ratcliff, J. T., G. Schubert, and A. Zebib (1996b), Effects of temperature-dependent viscosity on thermal convection in a spherical shell, *Phys. D*, *97*(1–3), 242–252.
Richter, F. M. (1973), Finite amplitude convection through a phase boundary, *Geophys. J. R. Astron. Soc.*, *35*, 265–276.
Rubie, D. C. (1984), The olivine → spinel transformation and the rheology of subducting lithosphere, *Nature*, *308*, 505–508.
Sammis, C. G., and J. L. Dein (1974), On the possibility of transformational superplasticity in the Earth's mantle, *J. Geophys. Res.*, *79*, 2961–2965, doi:10.1029/JB079i020p02961.
Sauveur, A. (1924), What is steel? Another answer, *Iron Age*, *113*, 581–583.
Schmeling, H., G. Marquart, and T. Ruedas (2003), Pressure and temperature-dependent thermal expansivity and the effect on mantle convection and surface observables, *Geophys. J. Int.*, *154*, 224–229.
Shahnas, M. H., and G. Jarvis (2007), On the relative importance of mineral phase transitions and viscosity stratification in controlling the sinking rates of detached slab remnants, *Geophys. Res. Lett.*, *34*, L11302, doi:10.1029/2007GL029463.
Shahnas, M. H., and W. R. Peltier (2010), Layered convection and the impacts of the perovskite-post perovskite phase transition on mantle dynamics under isochemical conditions, *J. Geophys. Res.*, *115*, B11408, doi:10.1029/2009JB007199.
Shahnas, M. H., J. P. Lowman, G. T. Jarvis, and H. P. Bunge (2008), Convection in a spherical shell heated by an isothermal core and internal sources: Implications for the thermal state of planetary mantles, *Phys. Earth Planet. Inter.*, *168*, 6–15.
Shahnas, M. H., W. R. Peltier, Z. Wu, and R. Wentzcovitch (2011), The high pressure electronic spin transition in iron: Potential impacts upon mantle mixing, *J. Geophys. Res.*, *116*, B08205, doi:10.1029/2010JB007965.
Shannon, R. D., and C. T. Prewitt (1969), Effective ionic radii in oxides and fluorides, *Acta Crystallogr., Sect. B*, *25*, 925–946, doi:10.1107/S0567740869003220.
Sharp, H. N., and W. R. Peltier (1979), A thermal history model for the Earth with parameterized convection, *Geophys. J. R. Astron. Soc.*, *59*, 171–203.
Sherman, D. M. (1988), High-spin to low-spin transition of iron (II) oxides at high pressures: Possible effects on the physics and chemistry of the lower mantle, in *Structural and Magnetic Phase Transitions in Minerals*, *Advances in Physical Geochemistry*, vol. 7, edited by S. Ghose et al., pp. 113–128, Springer, New York.
Soldati, G., L. Boschi, F. Deschamps, and D. Giardini (2009), Inferring radial models of mantle viscosity from gravity (GRACE) data and an evolutionary algorithm, *Phys. Earth Planet. Inter.*, *176*, 19–32.
Solheim, L. P., and W. R. Peltier (1993), Mantle phase transitions and layered convection, *Can. J. Earth Sci.*, *30*, 881–892.
Solheim, L. P., and W. R. Peltier (1994a), Avalanche effects in phase transition modulated thermal convection: A model of Earth's mantle, *J. Geophys. Res.*, *99*(B4), 6997–7018, doi:10.1029/93JB02168.
Solheim, L. P., and W. R. Peltier (1994b), Phase boundary deflections at 660-km depth and episodically layered isochemical convection in the mantle, *J. Geophys. Res.*, *99*(B8), 15,861–15,875, doi:10.1029/94JB00730.
Sotin, C., and S. Labrosse (1999), Three-dimensional thermal convection in an iso-viscous, infinite Prandtl number fluid heated from within and from below: Applications to the transfer of heat through planetary mantles, *Phys. Earth Planet. Int.*, *112*, 171–190.
Staniforth, A., and J. Thuburn (2012), Horizontal grids for global weather and climate prediction models: A review, *Q. J. R. Meteorol. Soc.*, *138*, 1–26.
Steinberger, B., and R. J. O'Connell (1997), Changes of the Earth's rotation axis owing to advection of mantle density heterogeneities, *Nature*, *387*, 169–173.
Stemmer, K., H. Harder, and U. Hansen (2006), A new method to simulate convection with strongly temperature-dependent and pressure-dependent viscosity in a spherical shell: Applications to the Earth's mantle, *Phys. Earth Planet. Inter.*, *157*, 223–249.
Stixrude, L., and C. Lithgow-Bertelloni (2012), Geophysics and chemical heterogeneity in the mantle, *Annu. Rev. Earth Planet. Sci.*, *40*, 569–595.

Stuhne, G. R., and W. R. Peltier (1999), New icosahedral grid-point discretizations of the shallow water equations on the sphere, *J. Comput. Phys.*, *148*(1), 23–58.
Su, W., and A. M. Dziewonski (1997), Simultaneous inversion for 3-D variations in shear and bulk velocity in the mantle, *Phys. Earth Planet. Inter.*, *100*, 135–156.
Tabata, M., and A. Suzuki (2000), A stabilized finite element method for the Rayleigh-Bénard equations with infinite Prandtl number in a spherical shell, *Comput. Methods Appl. Mech. Eng.*, *190*, 387–402.
Tackley, P. J. (1993), Effects of strongly temperature dependent viscosity on time-dependent, 3-dimensional models of mantle convection, *Geophys. Res. Lett.*, *20*, 2187–2190, doi:10.1029/93GL02317.
Tackley, P. J. (1994), Three-dimensional models of mantle convection: Influence of phase transitions and temperature-dependent viscosity, PhD thesis, California Institute of Technology, Pasadena.
Tackley, P. J. (1998), Three-dimensional simulations of mantle convection with a thermochemical CMB boundary layer: D"?, in *The Core-Mantle Boundary Region*, edited by M. Gurnis et al., pp. 231–253, AGU, Washington, D. C.
Tackley, P. J. (2008), Modelling compressible mantle convection with large viscosity contrasts in a three-dimensional spherical shell using the yin-yang grid, *Phys. Earth Planet. Inter.*, *171*, 7–18.
Tackley, P. J., D. J. Stevenson, G. A. Glatzmaier, and G. Schubert (1993), Effects of an endothermic phase transition at 670 km depth in a spherical model of convection in the Earth's mantle, *Nature*, *361*, 699–704.
Tackley, P. J., D. J. Stevenson, G. A. Glatzmaier, and G. Schubert (1994), Effects of multiple phase transitions in a 3-dimensional spherical model of convection in Earth's mantle, *J. Geophys. Res.*, *99*(B8), 15,877–15,901, doi:10.1029/94JB00853.
Torrance, K. E., and D. L. Turcotte (1971), Thermal convection with large viscosity variations, *J. Fluid Mech.*, *47*, 113–125.
Trampert, J., F. Deschamps, J. Resovsky, and D. Yuen (2004), Probabilistic tomography maps chemical heterogeneities throughout the lower mantle, *Science*, *306*(5697), 853–856.
Turcotte, D. L., and E. R. Oxburgh (1967), Finite amplitude convection cells and continental drift, *J. Fluid Mech.*, *28*, 29–42.
van den Berg, A. P., D. A. Yuen, and J. R. Allwardt (2002), Non-linear effects from variable thermal conductivity and mantle internal heating: Implications for massive melting and secular cooling of the mantle, *Phys. Earth Planet. Inter.*, *129*, 359–375.
Van der Voo, R., W. Spakman, and H. Bijwaard (1999a), Mesozoic subducted slabs under Siberia, *Nature*, *397*, 246–249.
Van der Voo, R., W. Spakman, and H. Bijwaard (1999b), Tethyan subducted slabs under India, *Earth Planet. Sci. Lett.*, *171*, 7–20.
van Keken, P. E., D. A. Yuen, and A. P. van den Berg (1995), Dynamical influences of high viscosity in the lower mantle induced by the steep melting curve of perovskite, *J. Geophys. Res.*, *100*, 15,233–15,248, doi:10.1029/95JB00923.
Vilella, K., S.-H. Shim, C. G. Farnetani, and J. Badro (2014), Spin state transition and partitioning of iron: Effects on mantle dynamics, *Earth Planet. Sci. Lett.*, *417*, 57–66.
Weertman, J., and J. R. Weertman (1975), High temperature creep of rock and mantle viscosity, *Annu. Rev. Geophys.*, *3*, 293–316.
Wentzcovitch, R. M., T. Tsuchiya, and J. Tsuchiya (2006), $MgSiO_3$ post-perovskite at D″ conditions, *Proc. Natl. Acad. Sci. U.S.A.*, *103*(3), 543–546.
Wentzcovitch, R. M., J. F. Justo, Z. Wu, C. R. S. da Silva, D. Yuen, and D. Kohlstedt (2009), Anomalous compressibility of ferropericlase throughout the iron spin crossover, *Proc. Natl. Acad. Sci. U.S.A.*, *106*, 8447–8452.
Winter, H. H. (1977), *Viscous Dissipation Term in Energy Equations*, *American Institute of Chemical Engineers, Modular Instruction Series, Module C7.4*, American Institute of Chemical Engineers, New York.
Wu, Z., and R. M. Wentzcovitch (2014), Spin crossover in ferropericlase and velocity heterogeneities in the lower mantle, *Proc. Natl. Acad. Sci. U.S.A.*, *111*(29), 10,468–10,472.
Wu, Z., J. F. Justo, C. R. S. da Silva, S. de Gironcoli, and R. M. Wentzcovitch (2009), Anomalous thermodynamic properties in ferropericlase throughout its spin crossover transition, *Phys. Rev.*, *80*, 014409, doi:10.1103/PhysRevB.80.014409.
Wu, Z., J. F. Justo, and R. M. Wentzcovitch (2013), Elastic anomalies in a spin-crossover system: Ferropericlase at lower mantle conditions, *Phys. Rev. Lett.*, *110*(22), 228501.
Yoshida, M., and A. Kageyama (2004), Application of the Yin-Yang grid to a thermal convection of a Boussinesq fluid with infinite Prandtl number in a three-dimensional spherical shell, *Geophys. Res. Lett.*, *31*, L12609, doi:10.1029/2004GL019970.
Yuen, D. A., and W. R. Peltier (1980), Mantle plumes and the thermal stability of the layer, *Geophys. Res. Lett.*, *7*(9), 625–628, doi:10.1029/GL007i009p00625.
Zerr, A., and R. Boehler (1993), Melting of $(Mg,Fe)SiO_3$ perovskite to 625 kilobars: Indication of a high melting temperature in the lower mantle, *Science*, *262*, 553–555.
Zhang, S. X., and U. Christensen (1993), Some effects of lateral viscosity variations on geoid and surface velocities induced by density anomalies in the mantle, *Geophys. J. Int.*, *114*(3), 531–547.
Zhang, S. X., and D. A. Yuen (1996), Various influences on plumes and dynamics in time-dependent compressible mantle convection in 3-D spherical-shell, *Phys. Earth Planet. Inter.*, *94*(3–4), 241–267.
Zhong, S., M. T. Zuber, L. Moresi, and M. Gurnis (2000), Role of temperature-dependent viscosity and surface plates in spherical shell models of mantle convection, *J. Geophys. Res.*, *105*(B5), 11,063–11,082, doi:10.1029/2000JB900003.
Zhong, S., A. K. McNamara, E. Tan, L. Moresi, and M. Gurnis (2008), A benchmark study on mantle convection in a 3-D spherical shell using CitcomS, *Geochem. Geophys. Geosyst.*, *9*, Q10017, 1525–2027, doi:10.1029/2008GC002048.